# Variational phase-field fracture approach for non-isothermal CO<sub>2</sub>-water two-phase flow in deformable porous media

Yuhao Liu<sup>a,b</sup>, Keita Yoshioka<sup>c,d</sup>, Tao You<sup>c,d</sup>, Hanzhang Li<sup>a,b</sup>, Fengshou Zhang<sup>a,b</sup>

<sup>a</sup>State Key Laboratory of Disaster Reduction in Civil Engineering, Tongji University, Shanghai 200092, China <sup>b</sup>Department of Geotechnical Engineering, College of Civil Engineering, Tongji University, Shanghai 200092, China

<sup>c</sup>Department Geoenergy, Technical University Leoben, Leoben 8700, Austria <sup>d</sup>Department of Environmental Informatics, Helmholtz Centre for Environmental Research - UFZ, Leipzig 04318, Germany

#### Abstract

When CO<sub>2</sub> is injected to induce fracture in rock, the fracture tends to propagate in a more complex pattern and at a lower critical pressure compared to water injection. This study presents a fracture propagation model under CO<sub>2</sub>-water two-phase flow, based on the variational thermo-hydro-mechanical phase-field approach. For each constituent (water and CO<sub>2</sub>), the mass balance equation is derived while accounting for the capillary effect and the respective equations of state. Meanwhile, the equivalent pressure from two fluids modifies the potential energy description in thermo-poroelastic media, following our previous micromechanics based model. The proposed model has been verified against the analytical solutions for one-dimensional incompressible, immiscible two-phase flow, and plane strain hydraulic fracture propagation, known as the KGD fracture. Our numerical experiments indicate that fractures propagate at lower breakdown pressures under supercritical CO<sub>2</sub> injection, and their paths are more influenced more by pre-existing weak interfaces due to low viscosity of CO<sub>2</sub>.

Keywords: Phase-field; Hydraulic fracturing; Thermo-hydro-mechanical coupling; Two-phase flow; Fixed stress split

# 3 1. Introduction

24

25

26

27

28

30

In reservoir stimulation for geothermal and hydrocarbon energy production, fluid injection is required to improve efficiency (Qun et al., 2019), prevent induced seisimicity (Bai et al., 2016), and ensure injected fluid containment (Basu et al., 2015). Gao et al. (2024) provided a comprehensive review of field applications of fracturing by CO<sub>2</sub> injection. While hydraulic fracturing remains a widely used reservoir stimulation technique, it faces challenges such as high water consumption (Chen and Carter, 2016), risks of subsurface contamination (Vengosh et al., 2014), and the potential to induce seismicity (Schultz et al., 2020). To address these issues, CO<sub>2</sub> fracturing has emerged as a promising waterless alternative (Zhang et al., 2022; Nianyin et al., 2021; Moridis, 2017; Mojid et al., 2021; Zhang et al., 2021; Zhou and Zhang, 2020). Generally, when the formation depth exceeds 11m, the temperature and pressure surpass the critical values of CO<sub>2</sub> (304.12K and

Preprint submitted to Elsevier

May 19, 2025

7.377MPa), bringing it into a supercritical state (Span and Wagner, 1996; Yang et al., 2022). Compared to water-based fracturing fluids, CO<sub>2</sub> exhibits lower dynamic viscosity and higher diffusivity, which can facilitate the formation of more complex fracture geometries (Ishida et al., 2016; Wu et al., 2023; Xie et al., 2021). Its near-zero surface tension results in reduced flow resistance within the fracture, allowing it to reach the tip of the fracture more easily (Zhu et al., 2024). Furthermore, the lower formation breakdown pressure associated with CO<sub>2</sub> may help reduce the risk of fault reactivation (Song et al., 2019; Liu et al., 2017; Ishida et al., 2021), although its low viscosity also leads to greater fluid leak-off. In addition, such operations present an opportunity for the subsurface utilization and storage of CO<sub>2</sub> (Espinoza and Santamarina, 2010; Middleton et al., 2015).

35

36

38

39

40

41

42

44

48

49

50

51

53

54

55

57

59

61

63

65

69

70

71

72

73

74

76

Effective utilization of CO<sub>2</sub> in hydraulic fracturing requires a thorough understanding of the complex mechanisms governing fracture nucleation and propagation. While experimental investigations have explored various aspects of CO<sub>2</sub> fracturing through parametric studies (Zhang et al., 2017, 2019b; Zhou et al., 2018, 2019; Zou et al., 2018; Jiang et al., 2018), these efforts are often constrained by limitations in scale and the difficulty of replicating high-pressure and high-temperature subsurface conditions, which can be addressed by numerical modeling (Adachi et al., 2007; Yew and Weng, 2014). However, current numerical approaches still struggle to fully capture the coupled TH<sup>2</sup>M processes, where H<sup>2</sup> denotes the two-phase flow in the thermo-hydro-mechanical system (Grunwald et al., 2022). In deep subsurface environments, elevated confining pressures and in-situ stresses complicate fracture initiation (Zhou et al., 2024), while the presence of natural fractures contributes to more complex fracture geometries (Zhang et al., 2019a; Chen et al., 2018). Additionally, large temperature differences between the injected CO<sub>2</sub> and the surrounding formation may lower the critical pressure required for fracture propagation and lead to wider crack openings (Jiao et al., 2022; Luo et al., 2022). Importantly, injecting CO<sub>2</sub> into saturated porous media creates a two-phase fluid system of water and CO<sub>2</sub>, which which requireses the model to account for capillary effects (Maxwell, 1876), saturation distributions (Brown, 1951), and phase transitions such as evaporation, precipitation, and dissolution (Lu and Connell, 2014; Afanasyev, 2013; Matter and Kelemen, 2009).

Several studies have explored the numerical simulation of CO<sub>2</sub> fracturing. Yan et al. (2019, 2020) developed a finite element hydromechanical (HM) model to simulate supercritical CO<sub>2</sub> fracturing in coal seams, focusing on secondary fracturing triggered by blast loads from CO<sub>2</sub> phase transitions and dynamic interactions between multiple cracks (Yan et al., 2019, 2020). Liu et al. (2020) proposed a hybrid model that integrates unsteady fluid flow with a cohesive solid framework to investigate the fracturing mechanism of supercritical CO<sub>2</sub>. Guo et al. (2022) conducted a comprehensive parametric study of fracture propagation, incorporating various geomechanical and operational parameters within a damage mechanics framework. Additional simulations have examined thermal effects and the influence of CO<sub>2</sub> phase states on fracture evolution (Xiao et al., 2024). Despite these advancements, many existing models restrict fracture propagation to predefined paths and lack the capability to capture complex behaviors such as branching and merging. Moreover, representing fractures as sharp discontinuities poses significant challenges for accurate numerical modeling.

Phase-field modeling of fractures (Bourdin et al., 2000, 2008) has seen continuous advancement in the last couple of decades. The first applications of phase-field methods to fluid-driven fractures focused on elastic media (Bourdin et al., 2012; Chukwudozie et al., 2013), and were later extended to poroelastic media (Wheeler et al., 2014; Mikelić et al., 2015). Noii and Wick (2019) expanded the framework to incorporate thermo-hydro-mechanical (THM) coupling. Since then, a growing body of research has developed THM phase-field models (Wang et al., 2023; Li et al., 2021; Yi et al., 2024a; Suh and Sun, 2021; Liu et al., 2024a; Lee et al., 2025b,a), with some models integrating

reactive transport and chemical effects (Dai et al., 2024). Other studies have focused on phase-field modeling of drying-induced fractures in partially saturated porous media (Heider and Sun, 2020; Cajuhi et al., 2018). Yi et al. (2024b) also proposed a coupled phase-field model for a water-oil mixture to predict residual oil saturation.

Regarding phase-field modeling of CO<sub>2</sub> fracturing, Xu et al. (2022) proposed a new energy release rate criterion for rock to simulate supercritical CO<sub>2</sub> fractures under hydro-mechanical (HM) coupling. Feng et al. (2021; 2023) extended this work to include thermo-hydro-mechanical (THM) processes, investigating thermal effects during CO<sub>2</sub> fracturing and validating their results against experimental data. Jiang et al. (2025) analyzed the influence of stress anisotropy on fracture morphology by injecting CO<sub>2</sub> into thermo-poro-elastic media. Despite these advances, current studies still fall short of modeling the complete TH<sup>2</sup>M fracturing process. The behavior of two-phase fluid flow within the hydraulic process remains insufficiently understood within the THM framework, and phase-field formulations for hydraulic and thermal parameters require further refinement. Additionally, solution algorithms for thermo-hydro-mechanical phase-field fracture models must ensure both efficiency and stability when coupled with two-phase flow.

In this study, we present a fully coupled TH<sup>2</sup>M phase-field fracture model for CO<sub>2</sub> fracturing. We extend our existing THM phase-field framework to incorporate CO<sub>2</sub>—water two-phase flow, involving two immiscible fluid phases. The mass balance equations for each fluid component are formulated with capillary pressure, where water is treated as the wetting phase and CO<sub>2</sub> as the non-wetting phase. Water saturation is determined through capillary pressure, while CO<sub>2</sub> density is computed as a function of pressure and temperature using an appropriate equation of state. A mixed-volume method is employed to compute equivalent hydraulic and thermal material properties. The degradation of thermo-poro-elastic strain energy is governed by a micromechanically derived Biot coefficient, which itself is a function of the phase-field variable (representing damage) and the adopted energy decomposition scheme. Pore fluid energy is reformulated using an equivalent liquid pressure to improve accuracy. To solve the coupled system, we adopt a hybrid monolithic-staggered scheme in which the non-wetting phase pressure and capillary pressure are solved simultaneously in a single iteration step. For the thermal stress analysis, we apply a stabilized fixed-stress split method to enhance numerical robustness.

Section 3 introduces the numerical implementation, including a mixed solution scheme and an adapted fixed-stress split method. In section 4 the proposed model is verified against analytical solutions for one-dimensional two-phase flow in porous media (McWhorter problem) and fluid-driven fracture propagation (KGD problem). Section 5 compares water-based and CO<sub>2</sub> fracturing in terms of single-fracture propagation and investigates CO<sub>2</sub> injection under various temperature differences. Finally, the interaction of hydraulic fractures with weak interfaces—under both water-based and CO<sub>2</sub> injection—is discussed, followed by conclusions and directions for future research.

We use the following notations throughout the paper. The second-order identity tensor is denoted by **I**. The trace operator  $\text{Tr}(\cdot)$  acting on the second-order tensors **A** is defined as  $\text{Tr}(\mathbf{A}) = \boldsymbol{\delta} : \mathbf{A}$ .  $\nabla(\cdot)$  is the gradient of  $(\cdot)$ . A repeated index in subscript follows Einstein's summation convention i.e.,  $a_ib_i = a_1b_1 + a_2b_2 + a_3b_3$  for i = 1,2,3. However, this convention is ignored for an index in parentheses, e.g.,  $a_{(i)}b_{(i)}$ .

### 2. Mathematical model

Consider a thermo-poro-elastic medium that occupies the domain  $\Omega \subset \mathbb{R}^d$ , d = 2, 3. In  $\Omega$ , a lower dimensional set of fractures is denoted by  $\Gamma$  (Fig. 1). The body is subjected to a possible flux  $\bar{\mathbf{q}}$ 

and a surface force  $\bar{\mathbf{t}}$  on the boundary  $\partial_N \Omega := \mathcal{C}_N \cup \partial \Gamma$ , where  $\mathcal{C}_N$  denotes the outer domain boundary and  $\partial \Gamma$  the fracture boundary. The prescribed displacement  $\bar{\mathbf{u}}$ , pressure  $\bar{\mathbf{p}}$  and temperature  $\bar{\mathbf{T}}$  can be applied on the boundary  $\partial_D \Omega$ . A mixture fluid of component L and component C is considered. No phase transition is considered; therefore, the two components will each remain in their respective phases. Furthermore, we assume a local thermal equilibrium in the domain in which the fluid and porous solid temperatures are equilibrated. The underlying study proceeds from the triphasic porous material, consisting of a solid phase (S) and two fluid phases (L and C). Regarding their wetting properties, we consider phase L as the wetting phase and phase C as the non-wetting phase. The mass density ias given as  $\rho_{\alpha} = \phi_{\alpha} \rho_{\alpha R} = \phi S_{\alpha} \rho_{\alpha R}$  ( $\alpha \in \{S, L, C\}$ ) where  $\phi$  is the porosity,  $S_{\alpha}$  is the saturation of phase  $\alpha$  and  $\beta$  and  $\beta$  is the intrinsic density. The phase volume fraction  $\phi_{\alpha} = \phi S_{\alpha}$ , where  $S_S = 1$ ,  $S_L + S_C = 1$ ,  $\phi_L + \phi_C = \phi$ .

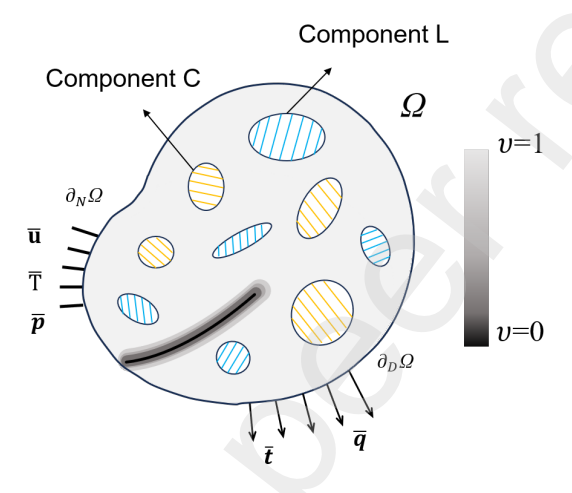


Fig. 1 Schematic of thermo-poroelastic medium with two-phase flow.

## 2.1. Mechanical equilibrium

The total energy  $\mathcal{E}_{\Gamma}$  of a homogeneous isotropic and linearly elastic material with a set of fractures is defined as a sum of the strain energy and the surface energy of fracture:

$$\mathcal{E}_{\Gamma}(\varepsilon(\mathbf{u}), \Gamma) := \int_{\Omega \setminus \Gamma} \psi(\varepsilon(\mathbf{u})) \, \mathrm{d}V + \int_{\Gamma} G_c \, \mathrm{d}S. \tag{1}$$

To alleviate the implementational difficulties of the discrete crack, we follow the work of Bourdin et al. (2000) to regularize the discrete cracks with a phase-field variable v that represents a state of the material from intact (v = 1) to fully broken (v = 0) (Fig.1). The total energy of a homogeneous isotropic and linearly elastic material  $\mathcal{E}$  is regularized as

$$\mathcal{E}(\varepsilon(\mathbf{u}), v) := \int_{\Omega} \psi(\varepsilon(\mathbf{u}), v) \, dV + \int_{\Omega} \frac{G_c}{4c_n} \left[ \frac{(1-v)^n}{\ell} + \ell \nabla v \cdot \nabla v \right] \, dV, \tag{2}$$

where  $\varepsilon$  is the total strain,  $G_c$  is the critical energy release rate and  $c_n$  is the normalizing parameter defined as  $c_n = \int_0^1 (1-s)^{n/2} S$ . For n=1 and n=2, the model is called  $AT_1$  model and  $AT_2$  model.

Also,  $\ell$  is the characteristic parameter with the dimension of a length that controls the phasefield profile transition. The strain energy density  $\psi(\varepsilon(\mathbf{u}), v)$  in Eq. (2) acknowledges the phase-field variable v and is continuous over  $\Omega$  for integration. Accounting for the thermo-poro-elastic medium, the energy functional can be extended to

$$\mathcal{E}(\varepsilon(\mathbf{u}), \zeta, T, v) := \int_{\Omega} \psi_{e}(\varepsilon(\mathbf{u}), T, v) \, dV + \int_{\Omega} \psi_{f}(\varepsilon(\mathbf{u}), \zeta, v) \, dV + \int_{\Omega} \psi_{T}(T) \, dV + \int_{\Omega} \frac{G_{c}}{4c_{n}} \left[ \frac{(1-v)^{n}}{\ell} + \ell \nabla v \cdot \nabla v \right] \, dV.$$
(3)

 $\mathbf{u}$ , p, and T represent the displacement, the pressure and temperature field, while  $\zeta$  denotes the incremental content of fluid. The total strain energy density  $\psi$  is assumed to be decomposed into elastic  $\psi_e(\varepsilon(\mathbf{u}), T, v)$  and hydraulic energies  $\psi_f(\varepsilon(\mathbf{u}), \zeta, v)$ . Furthermore, we assume that the thermal energy density  $\psi_T(T)$  is not contributed by mechanical or hydraulic processes (Suh and Sun, 2021).

With a degradation function  $g(v)^1$ , the elastic strain energy is contributed by the elastic strain  $\varepsilon_e$  acting on the solid skeleton so that

$$\psi_{e}(\varepsilon(\mathbf{u}), v, T) = g(v)\psi_{+}(\mathbf{u}) + \psi_{-}(\mathbf{u}) 
= \frac{1}{2}g(v)\mathbb{C}_{+} : \varepsilon_{e} : \varepsilon_{e} + \frac{1}{2}\mathbb{C}_{-} : \varepsilon_{e} : \varepsilon_{e} 
= \frac{1}{2}\mathbb{C}_{\text{eff}} : \varepsilon_{e} : \varepsilon_{e} 
= \frac{1}{2}\mathbb{C}_{\text{eff}} : \left(\varepsilon(\mathbf{u}) - \beta\Delta T\mathbf{I}\right) : \left(\varepsilon(\mathbf{u}) - \beta\Delta T\mathbf{I}\right),$$
(4)

155 where

158

161

150

152

153

$$\mathbb{C}_{\text{eff}} = g(v)\mathbb{C}_{+} + \mathbb{C}_{-}. \tag{5}$$

Here the expression for  $\mathbb{C}_{\text{eff}}$  is determined by no-tension model (Freddi and Royer-Carfagni, 2010). The total stress can be found by taking the derivative of  $\mathcal{E}$  with respect to  $\varepsilon_e$  as

$$\sigma = \mathbb{C}_{\text{eff}} : \varepsilon(\mathbf{u}) - \alpha(\upsilon) p_{FR} \mathbf{I} - 3\beta K_{\text{eff}} \Delta T \mathbf{I}, \tag{6}$$

where K is the drained bulk modulus. The total strain  $\varepsilon$  is decomposed into the elastic strain and the thermal strain which equals the product of thermal expansion coefficient  $\beta$  and the temperature difference  $\Delta T$  between the current temperature and initial temperature.  $\alpha(v)$  and  $K_{\rm eff}$  are the effective Biot's coefficient and the effective bulk modulus. Following the work by You and Yoshioka (2023), the effective Biot coefficient is given as

$$\alpha(v) = 1 - \frac{K_{\text{eff}}}{K_s}.\tag{7}$$

where  $K_s$  is the intrinsic bulk modulus. The effective bulk modulus depends not only on the damage

<sup>&</sup>lt;sup>1</sup>In this study, we employed  $g(v) = (1-k)v^2 + k$  where k is a phase-field parameter representing residual stiffness, which keeps the system of equations well-conditioned for the partly-broken state.

(v) but also on the type of energy decomposition scheme applied. The expression of  $K_{\rm eff}$  for the volumetric-deviatoric energy decomposition (Amor et al., 2009) is given by You and Yoshioka (2023), and the general expression of  $K_{\rm eff}$  can also be obtained with the expression of  $\mathbb{C}_{\rm eff}(v)$  and spherical projection  $\mathbf{P}_{\rm sph} = \frac{1}{3}\mathbf{I}$  as

$$K_{\text{eff}}(v) = \frac{1}{9} \text{Tr}(\mathbf{P}_{\text{sph}} : \mathbb{C}_{\text{eff}}(v) : \mathbf{I}). \tag{8}$$

By defining the degradation coefficient  $g_k$  with the initial bulk modulus K as

$$g_k = K_{\text{eff}}(v)/K,\tag{9}$$

we can rewrite effective Biot's coefficient in Eq. (7) as

$$\alpha(v) = 1 - \frac{K_{\text{eff}}(v)}{K_s} = 1 - K_{\text{eff}}(v) \frac{1 - \alpha_m}{K} = 1 - g_k (1 - \alpha_m)$$
(10)

where  $\alpha_m$  is the initial Biot's coefficient.

171

The hydraulic energy of pore fluid  $\psi_f$  is given as

$$\psi_f(\mathbf{u}, v, \zeta) = \frac{M_p}{2} \left[ \alpha(v) \text{Tr}(\varepsilon_{\mathbf{e}}) - \zeta \right]^2, \tag{11}$$

where  $M_p$  denotes the Biot's modulus as

$$\frac{1}{M_p} = \frac{\alpha(\nu) - \phi}{K_s},\tag{12}$$

The porosity depends on the deformation as

$$\phi = \phi_m + \varepsilon_1,\tag{13}$$

where  $\phi_m$  is the original porosity and  $\varepsilon_1$  is the maximum principal strain (Liu et al., 2024b). The incremental content of fluid  $\zeta$  is defined without the effect of thermal expansion as

$$\zeta = \alpha(v) \text{Tr}(\varepsilon_e) + \frac{p_{FR}}{M_p} \tag{14}$$

where  $p_{FR}$  is the equivalent fluid pressure defined as

$$p_{FR} = S_C p_{CR} + S_L p_{LR},\tag{15}$$

and  $p_{CR}$  and  $p_{LR}$  are the non-wetting phase pressure and total fluid pressure. The capillary pressure is defined as the difference between  $p_{CR}$  and  $p_{LR}$ 

$$p_c = p_{CR} - p_{LR}. (16)$$

The thermal energy  $\psi_T$  is assumed not to be contributed by mechanical and hydraulic process (Suh and Sun, 2021):

$$\psi_T(T) = (\rho c)_m \left[ (T - T_{\text{ref}}) - T \ln \left( \frac{T}{T_{\text{ref}}} \right) \right], \tag{17}$$

where  $T_{\rm ref}$  is the reference temperature.  $(\rho c)_m$  is the equivalent heat storage for porous medium given by

$$(\rho c)_m = \phi_L c_{p,L} \rho_{LR} + \phi_C c_{p,C} \rho_{CR} + (1 - \phi) c_{p,S} \rho_{SR}, \tag{18}$$

where  $c_{p,\alpha}$   $\alpha \in \{S, L, C\}$  is the specific heat capacity of each phase.

2.2. Fluid mass balance

The mass balance equation of each constituent can be expressed as

$$(\rho_{\alpha})_{S}' + \nabla \cdot (\rho_{\alpha} \mathbf{v}_{\alpha}) = \hat{p}_{\alpha}, \tag{19}$$

where  $\rho_{\alpha}$  is the mass density of phase  $\alpha$ ,  $(\bullet)'_s$  denotes the material time derivative of a quantity  $\bullet$  with respect to the velocity of the solid skeleton,  $\mathbf{v}_{\alpha}$  is the velocity of phase  $\alpha$ , and  $\hat{p}_{\alpha}$  is the mass production term. Accounting for the relative velocity of the fluid with respect to the solid skeleton, we yield

$$(\rho_{\alpha})_{S}' + \rho_{\alpha} \nabla \cdot \mathbf{v}_{S} + \nabla \cdot [\rho_{\alpha} (\mathbf{v}_{\alpha} - \mathbf{v}_{S})] = \hat{p}_{\alpha}, \tag{20}$$

where  $\mathbf{v}_s$  is the velocity of solid skeleton.

For the solid phase ( $\alpha = s$ ), no mass transfer to the solid phase occurs so that  $\hat{p}_{\alpha} = 0$ . Thus, the mass balance equation of solid phase simplifies to

$$(\rho_S)_S' + \rho_S \nabla \cdot (\mathbf{u})_S' = 0. \tag{21}$$

For a water component (L) and a  $CO_2$  component (C), their mass balances write

$$(\rho_L)_S' + \rho_L \nabla \cdot (\mathbf{u})_S' + \nabla \cdot [\rho_L(\mathbf{v}_L - \mathbf{v}_S)] = Q_L, \tag{22}$$

194 and

185

$$(\rho_C)_S' + \rho_C \nabla \cdot (\mathbf{u})_S' + \nabla \cdot [\rho_C(\mathbf{v}_C - \mathbf{v}_S)] = Q_C.$$
(23)

Eq. (22) can be expanded into

$$(nS_L \rho_{LR})_S' + nS_L \rho_{LR} \nabla \cdot (\mathbf{u})_S' + \nabla \cdot [\rho_L (\mathbf{v}_L - \mathbf{v}_S)] = Q_L.$$
(24)

Defining  $\rho_L(\mathbf{v}_L - \mathbf{v}_S) = \mathbf{q}_L$  as the advective liquid flux and neglecting the diffusive liquid flux Eq. (24) can be expanded into

$$S_L \rho_{LR}(n)_S' + n\rho_{LR}(S_L)_S' + nS_L(\rho_{LR})_S' + nS_L\rho_{LR}\nabla \cdot (\mathbf{u})_S' + \nabla \cdot \mathbf{q}_L = 0.$$
 (25)

Recalling Eq. (21), with  $S_S = 1$ , we have

$$((1 - \phi)\rho_{SR})'_S + (1 - \phi)\rho_{SR}\nabla \cdot (\mathbf{u})'_S$$
  
=  $(1 - \phi)(\rho_{SR})'_S - \rho_{SR}(\phi)'_S + (1 - \phi)\rho_{SR}\nabla \cdot (\mathbf{u})'_S = 0.$  (26)

Solving for the rate of porosity change yields

$$(\phi)_S' = (1 - \phi) \left( \frac{(\rho_{SR})_S'}{\rho_{SR}} + \nabla \cdot (\mathbf{u})_S' \right). \tag{27}$$

Substituting Eq. (27) into Eq. (25) gives

$$\phi \rho_{LR}(S_L)_S' + \phi S_L(\rho_{LR})_S' + S_L \rho_{LR} \frac{1 - \phi}{\rho_{SR}} (\rho_{SR})_S' + S_L \rho_{LR} \nabla \cdot (\mathbf{u})_S' + \nabla \cdot \mathbf{q}_L = Q_L.$$
 (28)

Similarly, we get the expanded mass balance of  $CO_2$  as

$$\phi \rho_{CR}(S_C)_S' + \phi S_C(\rho_{CR})_S' + S_C \rho_{CR} \frac{1 - \phi}{\rho_{SR}} (\rho_{SR})_S' + S_C \rho_{CR} \nabla \cdot (\mathbf{u})_S' + \nabla \cdot \mathbf{q}_C = Q_C.$$
 (29)

The rate of solid density change can be written as

208

$$\frac{(\rho_{SR})_S'}{\rho_{SR}} = \frac{1}{1 - \phi} \left[ (\alpha(\upsilon) - 1)\nabla \cdot (\mathbf{u})_S' - 3\beta(\alpha(\upsilon) - \phi)(T)_S' + \frac{\alpha(\upsilon) - \phi}{K_s} (p_{FR})_S' \right], \tag{30}$$

where  $\alpha(v)$  is Biot's coefficient,  $\beta$  is thermal expansive coefficient, T is global temperature and  $K_s$  is the intrinsic bulk modulus. Substituting Eq. (30) into Eq. (28), we obtain

$$S_{L}\rho_{LR}\left[(\alpha(v)-1)\nabla\cdot(\mathbf{u})_{S}'-3\beta(\alpha(v)-\phi)(T)_{S}'+\frac{\alpha(v)-\phi}{K_{S}}(p_{FR})_{S}'\right] + \phi\rho_{LR}(S_{L})_{S}'+\phi S_{L}(\rho_{LR})_{S}'+S_{L}\rho_{LR}\nabla\cdot(\mathbf{u})_{S}'+\nabla\cdot\mathbf{q}_{L}$$

$$=S_{L}\rho_{LR}\alpha(v)\nabla\cdot(\mathbf{u})_{S}'-3S_{L}\rho_{LR}\beta(\alpha(v)-\phi)(T)_{S}'+S_{L}\rho_{LR}\frac{\alpha(v)-\phi}{K_{S}}(p_{FR})_{S}'$$

$$+\phi\rho_{LR}(S_{L})_{S}'+\phi S_{L}(\rho_{LR})_{S}'+\nabla\cdot\mathbf{q}_{L}=Q_{L}.$$

$$(31)$$

Expanding the rate of equivalent pressure change with Eqs. (15) and (16), we have

$$(p_{FR})'_{S} = (S_{C}p_{CR} + S_{L}p_{LR})'_{S}$$

$$= [(S_{L}p_{CR})'_{S} - (S_{L}p_{c})'_{S} + (S_{C}p_{CR})'_{S}]$$

$$= S_{L}(p_{CR})'_{S} - (S_{L})'_{S}p_{c} - (p_{c})'_{S}S_{L} + S_{C}(p_{CR})'_{S}$$

$$= (p_{CR})'_{S} - (S_{L})'_{S}p_{c} - (p_{c})'_{S}S_{L}.$$
(32)

As for advective terms  $\mathbf{q}_{\alpha}$  ( $\alpha \in \{L, C\}$ ), the seepage velocity relates to pressure changes through Darcy's law

$$\mathbf{q}_L = \phi_L(\mathbf{v}_L - \mathbf{v}_s) = -\frac{k_L^{rel} \mathbf{k}_s}{\mu_{LR}} (\nabla p_{LR} - \rho_{LR} \mathbf{b})$$
(33)

$$\mathbf{q}_C = \phi_C(\mathbf{v}_C - \mathbf{v}_s) = -\frac{k_C^{rel} \mathbf{k}_s}{\mu_{CR}} (\nabla p_{CR} - \rho_{LR} \mathbf{b})$$
(34)

where  $k_{\alpha}^{rel}$  is relative permeability, **k** is the intrinsic permeability of the porous medium,  $\mu_{\alpha R}$  is viscosity and **b** is the body force. The saturation and relative permeability are calculated by Brooks Corey model (Brooks, 1965):

$$S_L(p_c) = \begin{cases} S_L^{max}, & p_c \le p_b \\ \left(\frac{p_b}{p_c}\right)^{\lambda} \left(S_L^{max} - S_L^r\right) + S_L^r, & p_c > p_b \end{cases}$$

$$(35)$$

$$k_L^{rel} = (S_e)^{\frac{2+3\lambda}{\lambda}}, k_C^{rel} = (1 - S_e)^2 (1 - S_e^{\frac{2+\lambda}{\lambda}})$$
 (36)

$$S_e = \frac{S_L - S_L^r}{S_L^{max} - S_L^r} \tag{37}$$

where  $S_L^{max}$  and  $S_L^r$  represent the maximum and residual saturation of water and  $S_e$  the effective saturation.  $p_b$  in the saturation model is the entry pressure concerning with the density and Biot's coefficient while  $\lambda$  is Brooks Corey's pore size distribution index. Substituting Eqs. (32), (33) and (34) into Eqs. (28) and (29) leads to

$$\phi S_{L}(\rho_{LR})'_{S} + \alpha(\upsilon)S_{L}\rho_{LR}\nabla \cdot (\mathbf{u})'_{S} - 3\beta S_{L}\rho_{LR}(\alpha(\upsilon) - \phi)(T)'_{S} + n\rho_{LR}(S_{L})'_{S}$$

$$+ S_{L}\rho_{LR}\frac{\alpha(\upsilon) - \phi}{K_{s}}(p_{CR})'_{S} - S_{L}\rho_{LR}\frac{\alpha(\upsilon) - \phi}{K_{s}}(S_{L})'_{S}p_{c} - S_{L}\rho_{LR}\frac{\alpha(\upsilon) - \phi}{K_{s}}(p_{c})'_{S}S_{L}$$

$$-\nabla \cdot \left(\rho_{LR}\frac{k_{L}^{rel}\mathbf{k}_{s}}{\mu_{LR}}(\nabla p_{CR} - \nabla p_{c} - \rho_{LR}\mathbf{b})\right) = Q_{L}$$
(38)

 $\phi S_{C}(\rho_{CR})'_{S} + \alpha(\upsilon)S_{C}\rho_{CR}\nabla \cdot (\mathbf{u})'_{S} - 3\beta S_{C}\rho_{CR}(\alpha(\upsilon) - \phi)(T)'_{S} - \phi\rho_{CR}(S_{L})'_{S}$   $+ S_{C}\rho_{CR}\frac{\alpha(\upsilon) - \phi}{K_{s}}(p_{CR})'_{S} - S_{C}\rho_{CR}\frac{\alpha(\upsilon) - \phi}{K_{s}}(S_{L})'_{S}p_{c} - S_{C}\rho_{CR}\frac{\alpha(\upsilon) - \phi}{K_{s}}(p_{c})'_{S}S_{L}$   $-\nabla \cdot \left(\rho_{CR}\frac{k_{C}^{rel}\mathbf{k}_{s}}{\mu_{CR}}(\nabla p_{CR} - \rho_{CR}\mathbf{b})\right) = Q_{C}$ (39)

For the dependency of permeability on the fracture deformation, we employ the model from Liu et al. (2024b). The altered permeability should be anisotropic, accounting for the Poiseuille-type flow in fractures (Miehe et al., 2015; Miehe and Mauthe, 2016):

$$\mathbf{K} = \mathbf{k}_s \mathbf{I} + (1 - v)^{\xi} \frac{\omega^2}{12} \left( \mathbf{I} - \mathbf{n}_{\Gamma} \otimes \mathbf{n}_{\Gamma} \right), \tag{40}$$

where  $\xi \geq 1$  is a weighting exponent and  $\mathbf{n}_{\Gamma}$  is the fracture unit normal vector, and the fracture width  $\omega$  as calculated as

$$\omega = h_e \varepsilon_1,\tag{41}$$

where  $h_e$  is the element size. We refer to Liu et al. (2024a) for details of the width computation and its verification against fracture opening problems.

225 2.3. Energy balance

212

217

226

The energy conservation in porous medium is given as

$$3\beta K_{\text{eff}} T \nabla \cdot (\mathbf{u})_S' + (\rho c)_m \frac{\partial T}{\partial t} + \nabla \cdot (\mathbf{q}_T) = Q_T, \tag{42}$$

where the first term denotes the thermal effect due to the deformation and  $Q_T$  is the source term. We assume that the thermal dilation due to deformation is neglected.  $\mathbf{q}_T$  denotes the heat flux which is decomposed into advective and conductive terms using Fourier's law:

$$\mathbf{q}_T = \rho_{LR} \mathbf{q}_L c_{p,L} T + \rho_{CR} \mathbf{q}_C c_{p,C} T - \lambda_{\text{eff}} \nabla T, \tag{43}$$

where the effective thermal conductivity is the summation of the partial parts of solid skeleton, water and CO<sub>2</sub> weighted by porosity:

$$\lambda_{\text{eff}} = (1 - \phi)\lambda_s + \phi_L \lambda_L + \phi_C \lambda_C. \tag{44}$$

## 3. Numerical implementation

232

233

234

235

236

237

238

239

Our theoretical framework consists of four processes: the hydraulic, the thermal, the mechanical, and the phase-field evolution processes. These four processes involve five primary variables as the hydraulic process has the two mass balance equations for each component with non-wetting phase pressure  $p_{CR}$  and capillary pressure  $p_c$ . To solve all the primary variables, a nested staggered scheme is applied as outlined in Algorithm 1. A global loop is set between v and the sub-loop  $[T, [p_{CR}, p_c], u]$  where the two pressure variables  $(p_{CR}, p_c)$  are solved in a monolithic scheme because of their strong dependency. To stabilize the sub-loop, we adopt the fixed-stress splitting method (Kim et al., 2011) by freezing the volumetric stress in the hydraulic process. Detailed discretization forms are given in Appendix A.

# Algorithm 1 A staggered solution of TH<sup>2</sup>M phase-field modeling

**Require:** Tolerence:  $\delta_v$ ,  $\delta_T$ ,  $\delta_{p_c}$ ,  $\delta_{p_{CR}}$   $\delta_{\mathbf{u}}$ , maximum number of iteration for global loop  $m_{\max}^g$ , maximum number of iteration for subloop  $m_{\max}^s$ , total time step n etc.

**Ensure:** Displacement **u**, temperature T, capillary pressure  $p_c$ , non-wetting phase pressure  $p_{CR}$  and phase-field v.

```
1: for k \leftarrow 1 to n do
                /* Alternate minimization algorithm */
  2:
                while \Delta v \geq \delta_v and n \leq m_{\max}^g do
  3:
  4:
                       v^{k,n} = \mathbf{Step}_{-}v(T^{k,n-1}, p_c^{k,n-1}, p_{CR}^{k,n-1}, \mathbf{u}^{k,n-1});
  5:
                       {\bf UpdateFractutreWidth}({\bf u}, \upsilon);
  6:
                       \Delta v = |v^{k,n} - v^{k,n-1}|;
  7:
                       /* TH<sup>2</sup>M coupling algorithm */
  8:
                        \begin{aligned} \mathbf{while} \ \Delta T &\geq \delta_T, \ \Delta p_c \geq \delta_{p_c}, \Delta p_{CR} \geq \delta_{p_{CR}}, \ \Delta \mathbf{u} \geq \delta_{\mathbf{u}} \ \mathbf{and} \ m \leq m_{\max}^s \ \mathbf{do} \\ T^{k,m} &= \mathbf{Step\_T}(p_c^{k,m}, p_{CR}^{k,m}, v^{k,m}); \\ \Delta T &= |T^{k,m} - T^{k,m-1}|; \end{aligned} 
  9:
10:
11:
                              /* fixed stress splitting method*/
12:
                               \begin{array}{l} (p_c^{k,m},p_{CR}^{k,m}) = \mathbf{Step\_p}(T^{k,m},\mathbf{u}^{k,m-1},p_c^{k,m-1},p_{CR}^{k,m-1},\upsilon^{k,m}); \\ \Delta p_c = |p_c^{k,m}-p_c^{k,n-i}|; \end{array} 
13:
14:
                              \begin{split} &\Delta p_{CR} = |p_{CR}^{k,m} - p_{CR}^{k,n-i}|;\\ &\mathbf{u}^{k,m} = \mathbf{Step\_u}(T^{k,m}, p_{c}^{k,m}, p_{CR}^{k,m}, v^{k,m}); \end{split}
15:
16:
                              UpdateFractutreWidth(u, v);
                              \Delta \mathbf{u} = |\mathbf{u}^{k,m} - \mathbf{u}^{k,m-1}|;
18:
                              m = m + 1;
19:
20:
                       n = n + 1;
21:
22:
```

#### 4. Model verification

To the best of our knowledge, no closed-form solution is available for the non-isothermal fracture propagation with two-phase flow. Therefore, this section presents verifications of two subsets of the whole process: one-dimensional incompressible, immiscible two-phase flow problem and the plane strain hydraulic fracture propagation, i.e, KGD problem. For verification of the thermo-hydromechanical part, we refer to our previous work (Liu et al., 2024b).

#### 4.1. McWorther problem

Firstly, we verified the two-phase flow module against the analytical solution proposed by McWhorter and Sunada (1990). Fig. 2 illustrates the one-dimensional flow of two incompressible, immiscible fluids through a porous medium, where the wetting phase displaces the non-wetting fluid in the horizontal direction. The initial non-wetting phase pressure  $p_{GR}$  is 0.1 MPa and the initial saturation is 0.05. On the left boundary the saturation for the wetting phase is set to 0.8 with a fixed capillary pressure to displace the non-wetting phase. Other parameters are listed in Table 1. The saturation profile along the horizontal direction at t = 1000 s is shown in Fig. 3, which closely matches the analytical solution.

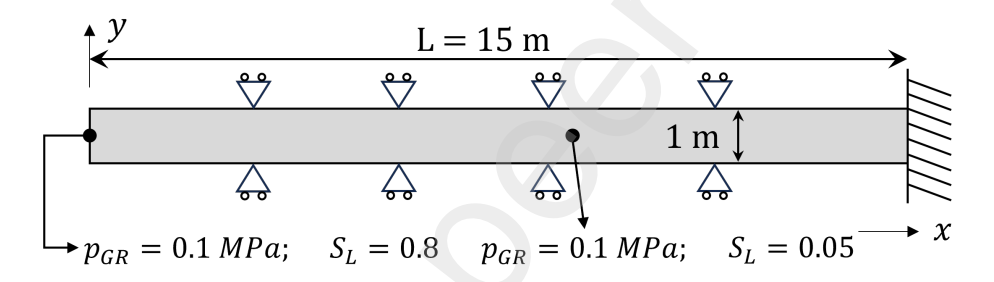


Fig. 2 Schematic of McWorther problem.

## 4.2. KGD problem

The second benchmark is to verify the hydromechanical module of our model with a propagating fracture (phase field) in the plane strain condition against a so-called KGD model (Kristianovich-Geertsma-de Klerk (Garagash, 2006)) without fluid leak-off. Assuming a symmetry over the y-axis, a line fracture  $[0 \text{ m}, 2 \text{ m}] \times \{30 \text{ m}\}$  is considered in a domain  $[0 \text{ m}, 45 \text{ m}] \times [0 \text{ m}, 60 \text{ m}]$  (Fig. 4). We consider the injection of an incompressible fluid  $(c_f = 0)$  into an impermeable elastic medium  $(\alpha_m = 0 \text{ and } \phi_m = 0)$  to induced propagation of the line fracture. Regarding the injected fluid as a wetting phase, we set the non-wetting phase pressure to 0 in the entire domain so that the fluid mass remains single-phase. The smallest element size is 0.05 m and  $\ell/h_e = 2$ . In the first 10 time steps,  $\Delta t = 0.01$  s and then  $\Delta t = 0.1$  s in the remaining simulation time. Table 2 lists the mechanical and flow parameters.

The hydraulic fracture propagation in this setting is considered a toughness-dominated regime (Detournay and Garagash, 2003) in which the fluid viscous dissipation is negligible compared to the energy release by fracture propagation. To judge the fracture propagation regime, we can use the

**Table 1** Parameters for McWorther problem.

Input parameters	Value	Unit
Porosity $(\phi_m)$	0.15	-
Intrinsic permeability $(\mathbf{k}_s)$	1e-10	$\mathrm{m}^2$
Residual saturation of wetting phase $(S_L^r)$	0.02	
Maximum saturation of wetting phase $(S_L^{max})$	0.999	-
Dynamic viscosity of wetting phase $(\mu_L)$	1e-3	Pa· s
Dynamic viscosity of non-wetting phase $(\mu_C)$	5e-3	$\mathrm{Pa\cdot\ s}$
Brooks and Corey model: entry pressure $(p_b)$	5000	Pa
Brooks and Corey model: pore size distribution index $(\lambda)$	3	-

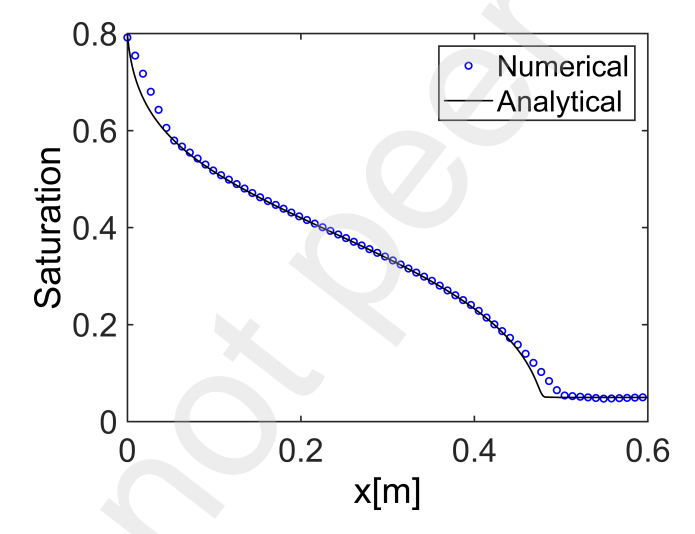


Fig. 3 Comparison of numerical solution and analytical solution of McWorther problem.

dimensionless viscosity  $\mathcal{M}$  defined for the KGD fracture as (Garagash, 2006)

$$\mathcal{M} = \frac{\mu' Q}{E'} \left(\frac{E'}{K'}\right)^4,\tag{45}$$

with  $K' = \sqrt{\frac{32G_c E'}{\pi}}$ ,  $\mu' = 12\mu$ ,  $E' = \frac{E}{1-\nu^2}$ . And if  $\mathcal{M} < \mathcal{M}_c = 3.4 \times 10^{-3}$ , the KGD fracture

is toughness dominated. In our setting,  $\mathcal{M}=3.8\times10^{-7}$  and  $\mathcal{M}<\mathcal{M}_c^2$ . Fig. 5 compares the numerical results against the analytical solution (Garagash, 2006). The pressure of injection point, fracture length and fracture width all demonstrate a good agreement.

Table 2 Mechanical and flow parameters for KGD problem.

Input parameters	Value	Unit
Young's modulus $(E)$	17	GPa
Poisson's ratio $(v)$	0.2	-
Permeability $(\mathbf{K}_m)$	$1\times10^{-18}$	$\mathrm{m}^2$
Fluid viscosity $(\mu)$	$1 \times 10^{-8}$	Pa·s
Injection rate $(Q)$	$2\times10^{-3}$	$\mathrm{m}^2/\mathrm{s}$
Critical surface energy release rate $(G_c)$	300	N/m

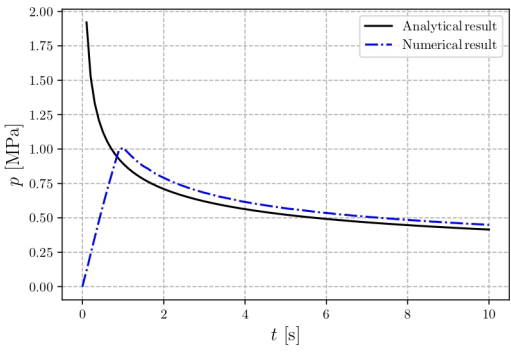
275

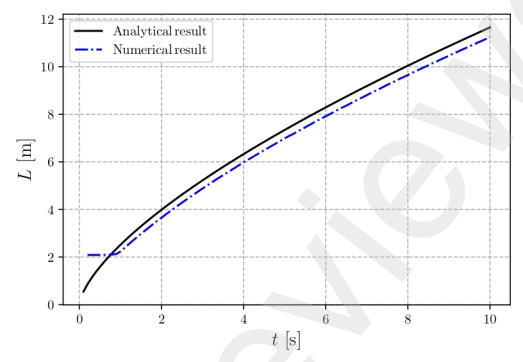
 $p_{FR} = 0$   $p_{FR} = 0$   $p_{FR} = 0$   $p_{FR} = 0$   $p_{FR} = 0$ 

Fig. 4 Schematic of KGD problem.

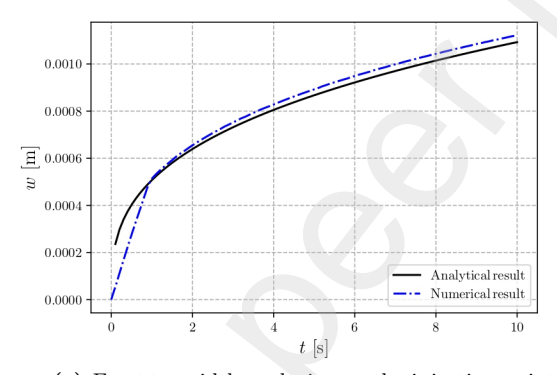
$$G_{\rm c}^{\rm eff} = G_{\rm c} \left( 1 + \frac{h_e}{4c_n \ell} \right).$$

<sup>&</sup>lt;sup>2</sup>The effective critical surface energy release rate  $G_c$  in the phase-field model needs to be adjusted to account for the discretization (Bourdin et al., 2008; Tanné et al., 2018; Yoshioka et al., 2020). With the mesh size  $h_e$  and the characteristic length  $\ell$ , the modification is given by





- (a) Pressure response at the injection point.
- (b) Fracture length evolution.



(c) Fracture width evolution at the injection point.

Fig. 5 Comparisons of numerical solutions and analytical solutions of KGD problem.

#### 5. Numerical experiments

277

278

279

280

281

282

283

284

286

287

In this section, we highlight the differences between water-based and CO<sub>2</sub>-based fracturing through a series of numerical experiments. We begin by comparing fracturing with the two fluids under isothermal conditions, followed by cases involving varying injection temperatures. Next, we emphasize the importance of two-phase flow modeling by comparing the two-phase flow model against a simulation of the same scenario based on a single-phase CO<sub>2</sub> flow assumption. Finally, we compare water-based and CO<sub>2</sub> fracturing in the presence of natural fractures. To capture the dependence of CO<sub>2</sub> density on temperature and pressure, we employ the Peng–Robinson equation of state (Peng and Robinson, 1976) (see Appendix Appendix A for details).

## 5.1. Comparison between water-based and supercirtical CO<sub>2</sub> fracturing

We simulated water and CO<sub>2</sub> injection into a pre-existing crack [3.98 m, 4.02 m]×{0 m} in the domain [0 m, 8 m]×[-2 m,2 m] (Fig. 6) with an injection rate of 2e-5 m<sup>2</sup>/s. The initial pressure in the domain is 15 MPa, and the in-situ stresses of  $\sigma_{xx} = 22$  MPa and  $\sigma_{yy} = 20$  MPa were imposed

through traction loadings on all the boundaries except y = 0, where the normal displacement was constrained. For hydraulic and thermal processes, all the boundaries were set as drained and isothermal conditions. Table 3 lists all the material properties in this example.

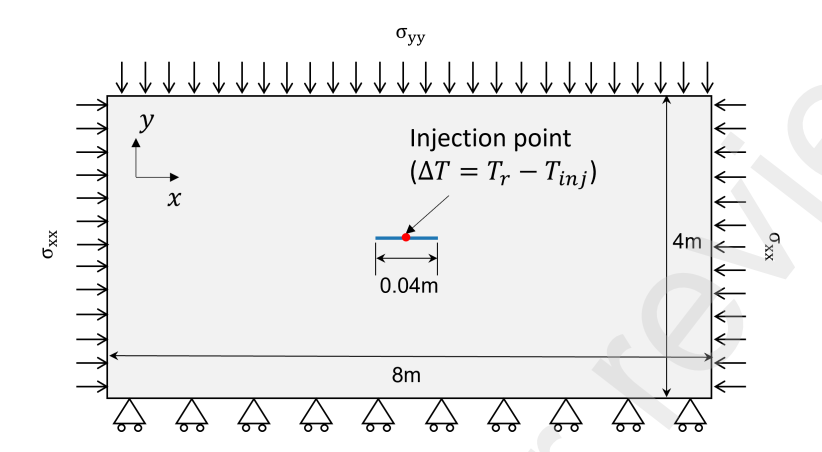


Fig. 6 The schematic of a single fracture in the middle of the domain.

Table 3 Parameters for single-cracked model.

Input parameters	Value	Unit
Young's modulus $(E)$	25	GPa
Poisson's ratio $(v)$	0.2	-
Biot's coefficient $(\alpha_m)$	0.6	-
Permeability $(\mathbf{K}_m)$	4e-16	$\mathrm{m}^2$
Thermal conductivity of solid, water and $\mathrm{CO}_2$ ( $\lambda$ )	3, 0.5, 0.03	$W/(m \cdot K)$
Thermal expansivity $(\alpha_s)$	$8 \times 10^{-6}$	-
Fluid viscosity of water and $CO_2$ ( $\mu$ )	$5 \times 10^{-4},  5 \times 10^{-5}$	$Pa \cdot s$
Critical surface energy release rate $(G_c)$	50	N/m
Initial temperature $(T_r)$	353.15	K
Injection temperature $(T_{inj})$	313.15	K

The first simulation cases compare water injection to  $CO_2$  injection under isothermal conditions, i.e.,  $\Delta T = 0$  (Fig 7). For the water injection case, the pressure reaches the critical pressure<sup>3</sup> (Fig 7a),

292

<sup>&</sup>lt;sup>3</sup>The critical pressure will be 31.2 MPa based on the analytical solution  $\left(\sigma_{yy} + \sqrt{\frac{E'G_c}{l_o\pi}}\right)$  (Bourdin et al., 2012),

<sup>294</sup> and the fracture begins to propagate (Fig. 7b). However, in the CO<sub>2</sub> injection case, the pressure does not build up enough even after 300 s, due to the low viscosity of CO<sub>2</sub> (Fig. 7), and the fracture does not grow (Fig. 7b).

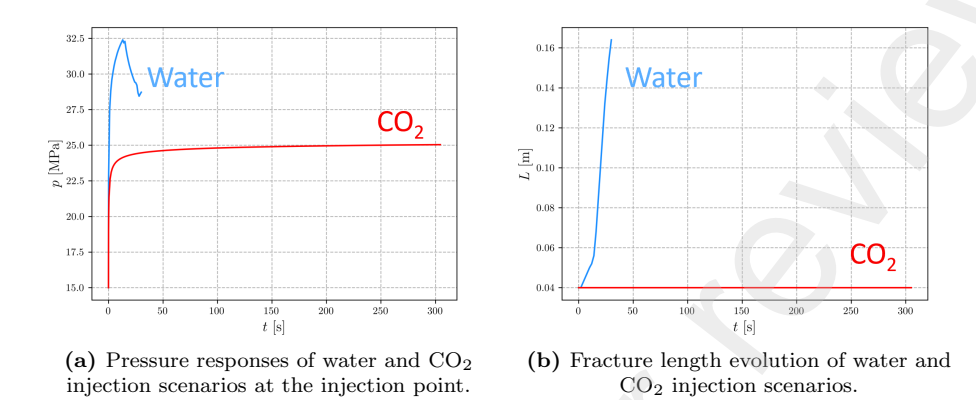


Fig. 7 Simulated pressure responses (a) and fracture length evolution (b) of water and CO<sub>2</sub> injection scenarios under isothermal condition.

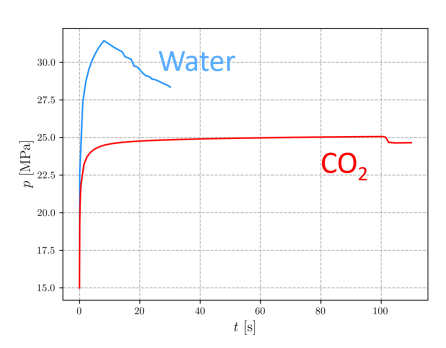
Next, we repeated the same simulations with a lower injection temperature of 313.15 K (i.e.,  $\Delta T = 40$  K). For the water injection case, the peak pressure is lower (Fig. 8) compared to the isothermal case, as the cold injection temperature causes the rock to contract, thereby reducing the compressive stress. Again, in  $CO_2$  injection case, the pressure does not build up as much as the water injection case. However, due to the cold injection fluid, the fracture begins to gradually propagate right from the beginning despite the subcritical fluid pressure build-up within the fracture. When its growth accelerates around 100 s, the injection pressure drops slightly.

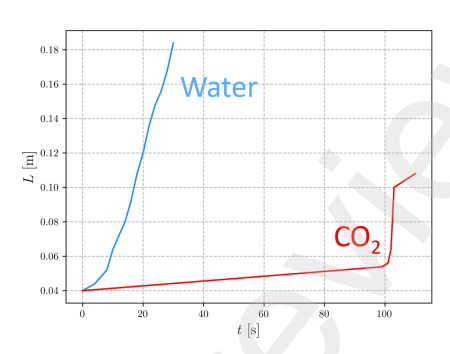
For the water injection case, the temperature decreases predominantly along the fracture while the reduced temperature profile is more diffused in the  $CO_2$  injection case due to the strong diffusion and the weak surface tension of  $CO_2$  (Fig. 9). Prior to the onset of fracture propagation,  $CO_2$  diffuses into the reservoir formation from the initial fracture. Once the fracture starts to propagate, the  $CO_2$  travels faster along the growing fracture, developing an advection-diffusion mixed  $CO_2$  saturation profile.

### 5.2. CO<sub>2</sub> fracturing under non-isothermal conditions

This section explores the fracturing behavior under  $CO_2$  injection at three different injection temperatures ( $\Delta T = 40 \text{ K}$ , 50 K, 60 K), using the same setup as in Sec. 5.1. As before, pressure does not build up significantly at the injection point (Fig. 10a), and no clear break-down is observed. However, whenever the pressure drops slightly (around 100 s for  $\Delta T = 40 \text{ K}$ , around 40 s for  $\Delta T = 50 \text{ K}$ , and around 30 s for  $\Delta T = 60 \text{ K}$  cases), the fracture growth accelerates similarly to the previous  $CO_2$  injection case. The greater the temperature difference ( $\Delta T$ ), the earlier the acceleration in

assuming no leak-off and infinite domain boundaries.





- (a) Pressure responses of water and CO<sub>2</sub> injection scenarios at the injection point.
- (b) Fracture length evolution of water and  $CO_2$  injection scenarios at the injection point.

Fig. 8 Simulated pressure responses (a) and fracture length evolution (b) of water and  $CO_2$  injection scenarios under non-isothermal condition.

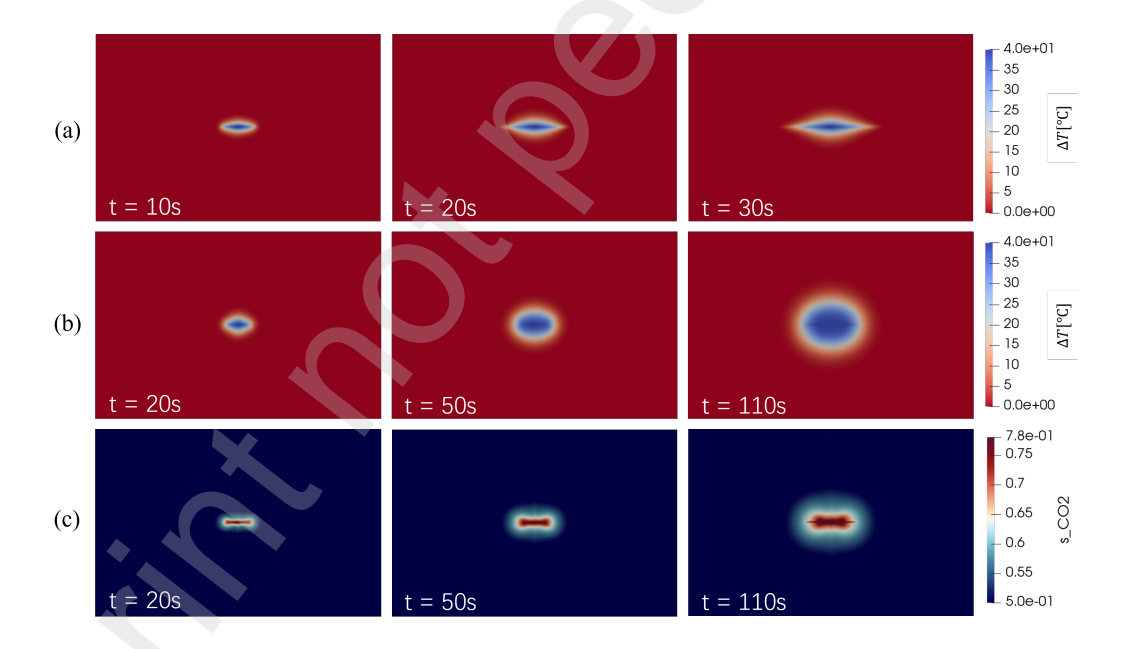
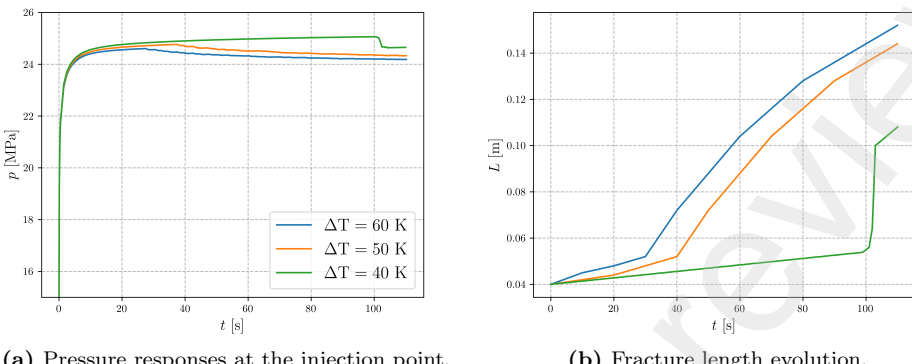


Fig. 9 Temperature difference ( $\Delta T$ ) profiles of (a) water injection and (b) CO<sub>2</sub> injection cases, and (c) CO<sub>2</sub> saturation profiles over time.

fracture propagation begins (Fig. 10b), and the wider the fracture openings are at the injection point (Fig. 10c).



(a) Pressure responses at the injection point.

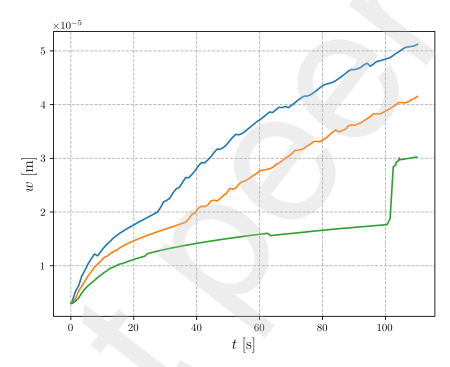
319

320

321

322

(b) Fracture length evolution.



(c) Fracture width evolution at the injection point.

Fig. 10 Simulated  $CO_2$  injection into a fracture under three different injection temperatures ( $\Delta T$ = 40 K, 50 K, 60 K).

With the increasing temperature difference, the mode of  $CO_2$  transport shifts from diffusiondominated to advection-dominated. As the fracture propagation accelerates, CO<sub>2</sub> transport becomes more strongly influenced by the fracture. This shift reduces the average CO<sub>2</sub> saturation in the reservoir, which may be beneficial in terms of CO<sub>2</sub> storage (Fig. 11).

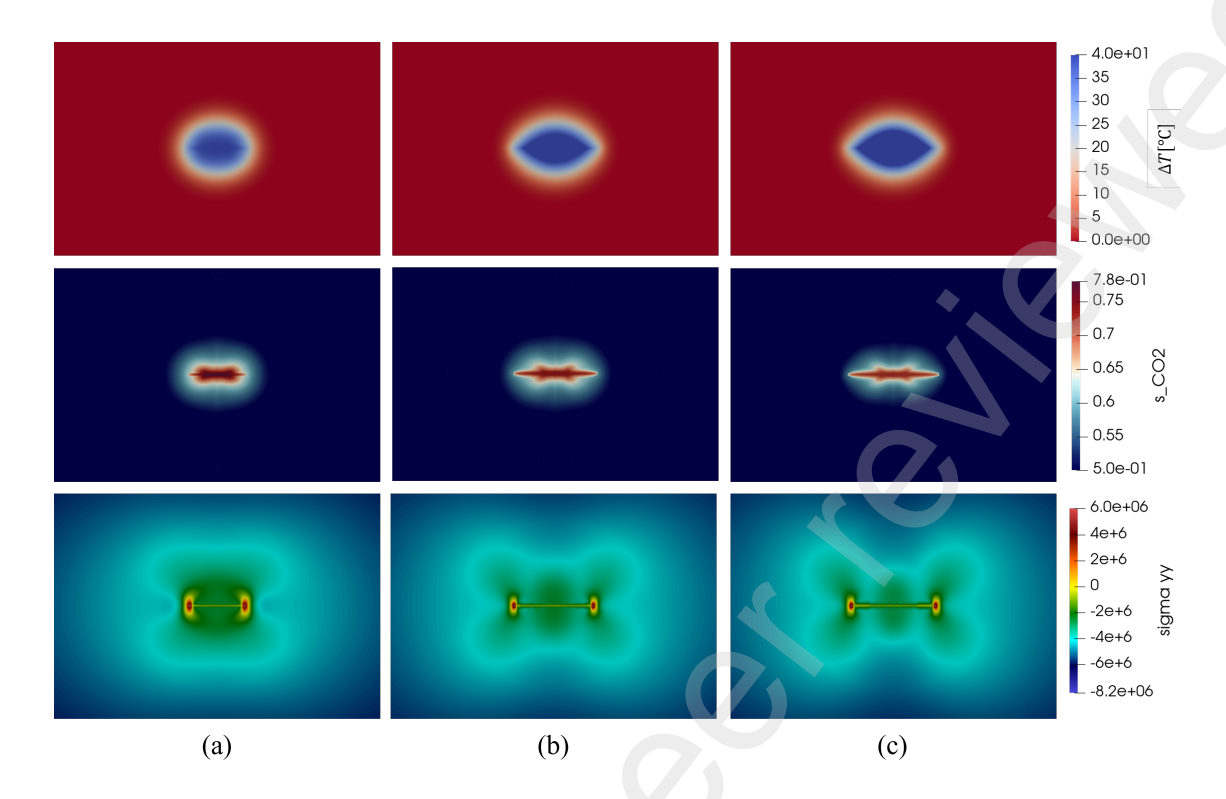


Fig. 11 Comparison of temperature, saturation and vertical stress distribution in the cases with  $\Delta T = 40 \text{ K}$  (a), 50 K (b) and 60 K (c) at the end of the simulation time (110 s).

Lower injection temperatures also reduce the effective stress along the propagating fracture in the y-direction (Fig. 10(c)). Compared to the reduction of effective stress during water fracturing discussed in (Liu et al., 2024a), the temperature decreases more near the tip of the fracture, which results from uniform thermal diffusion with low-viscosity fluid.

## 5.3. Two-phase flow effects

This section emphasizes the importance of properly modeling two-phase fluid flow by comparing it with a simplified single-phase flow model. Assuming single-phase  $\mathrm{CO}_2$  flow, we simulated the same fracturing scenarios using the parameters listed in Table 3 with a temperature difference of  $\Delta T=40~\mathrm{K}$ . In the single-phase case, the pressure build-up is significantly lower than in the two-phase flow scenario (Fig.12a), and fracture propagation does not occur (Fig.12b). This difference highlights a key aspect of  $\mathrm{CO}_2$  fracturing: as a low-viscosity, non-wetting phase,  $\mathrm{CO}_2$  injected into water-saturated porous media has a relative permeability much smaller than one as the water saturation is high in the beginning. This leads to a higher pressure required to induce fracture propagation. In contrast, the single-phase model neglects capillary effects, resulting in insufficient pressure to propagate the fracture.

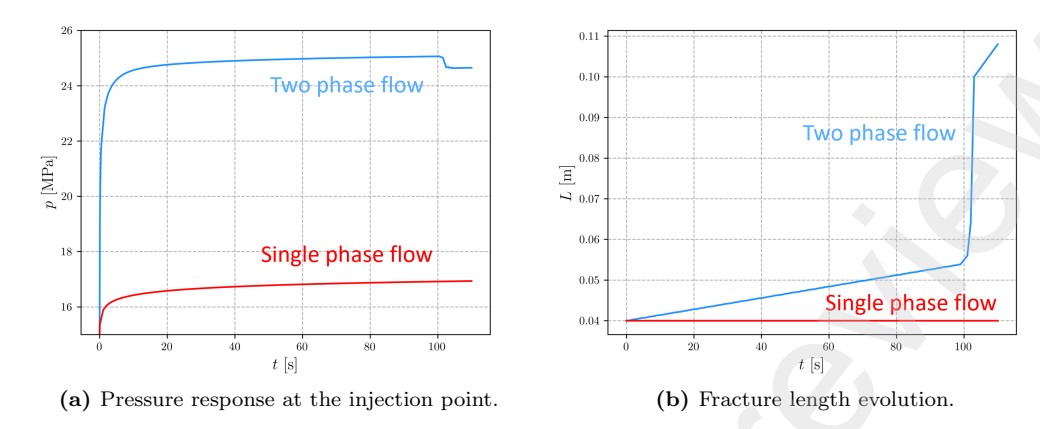


Fig. 12 Propagation of a single fracture under the assumptions of two phase and single phase flow.

#### 5.4. Interactions with weak interfaces

338

339

341

342

343

345

347

In this section, we highlight the differences between water and  $CO_2$  injection induced fracturing in the presence of weak interfaces (e.g., defects or natural fractures). Weak interfaces in our simulation were modeled as planes with reduced fracture toughness ( $G_c$ ), following the approach proposed by Yoshioka et al. (2020). As shown in Fig. 13, a weak interface is placed at each end of the initial crack, inclined at 45° to the x-direction. The fracture toughness of the weak interfaces is set to 40% of that of the bulk rock formation, and no frictional shear slippage is considered along the interfaces under compression. The in-situ stresses in the x- and y-directions ( $\sigma_{xx}$  and  $\sigma_{yy}$ ) are 23 MPa and 20 MPa, respectively. The temperature difference between the injection fluid and the reservoir formation is 50 K, and all other parameters are the same as the previous numerical examples.

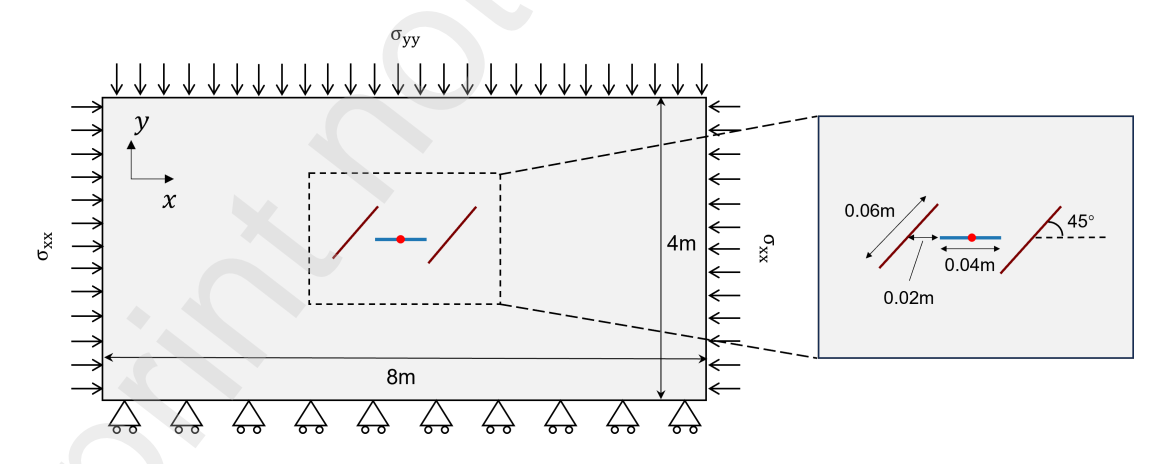


Fig. 13 The schematic of a single fracture with natural fractures.

Fig. 14 compares fracture interactions with weak interfaces in the water and CO<sub>2</sub> injection cases.

In the water injection case, fracture propagation is only slightly influenced by the interfaces, and the fracture essentially propagates straight through the interfaces (Fig.14(a)). With CO<sub>2</sub> injection, the fracture is more receptive to weak interfaces; its propagation is disturbed when encountering them (Fig.14(b)). In both cases, however, the stress differential (3MPa) is sufficient for the fractures to propagate in the direction of the maximum in-situ stress, i.e., the x-direction.

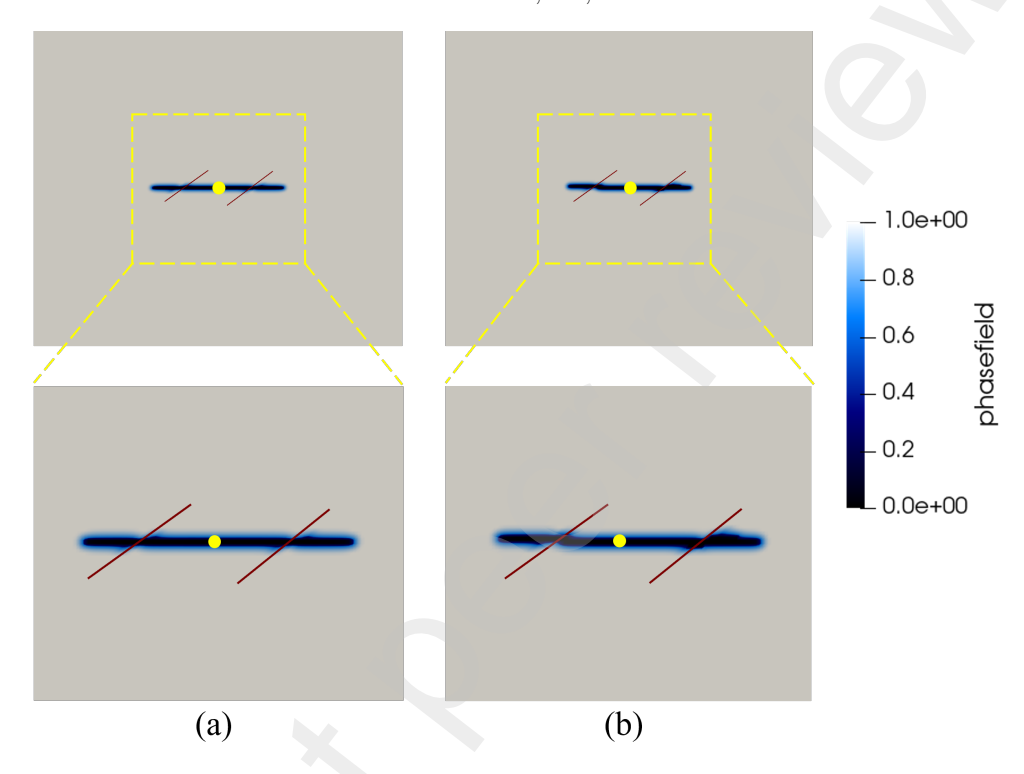


Fig. 14 The fracture interacting with weak interfaces in water (a) and CO<sub>2</sub> (b) fracturing.

When the fracture passes through the interface after approximately 12.5 s of water injection, the pressure drops after the peak while, in the  $CO_2$  fracturing, the pressure drops only slightly and exhibits oscillations which indicates the interaction with the natural fractures (Fig. 15).

The CO<sub>2</sub> injection simulation was repeated with the stress difference of 0 MPa. Fig. 16 shows that the fracture changes its direction when it hits the weak interfaces and propagates along the interfaces. The fracture also begins to propagate earlier with a lower critical pressure (Fig. 17).

The saturation profiles of  $CO_2$  under different stress differentials are compared in Fig.18. When interacting with natural fractures, the injected  $CO_2$  flows along the deflected fracture path (Fig.18(a)) and leaks into the branching fractures (Fig. 18(b)).

#### 6. Discussion

Our proposed numerical approach overcomes the limitations of previous models that relied on partially coupled hydro-mechanical (HM) formulations or assumed single-phase flow. By implementing a fully coupled TH<sup>2</sup>M framework, we enable a more realistic and comprehensive analysis

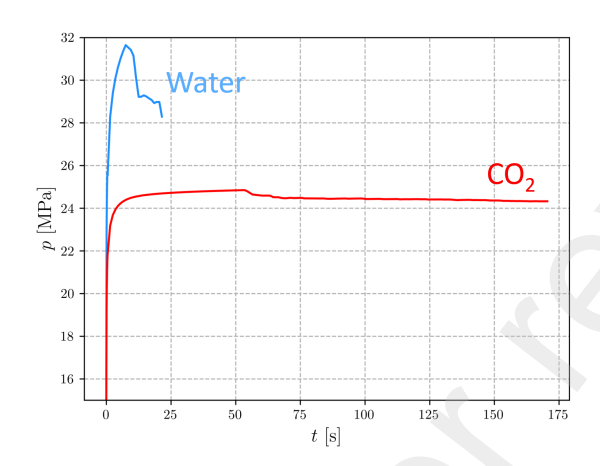


Fig. 15 Pressure response st injection point with weak interfaces in water and  ${\rm CO}_2$  fracturing.

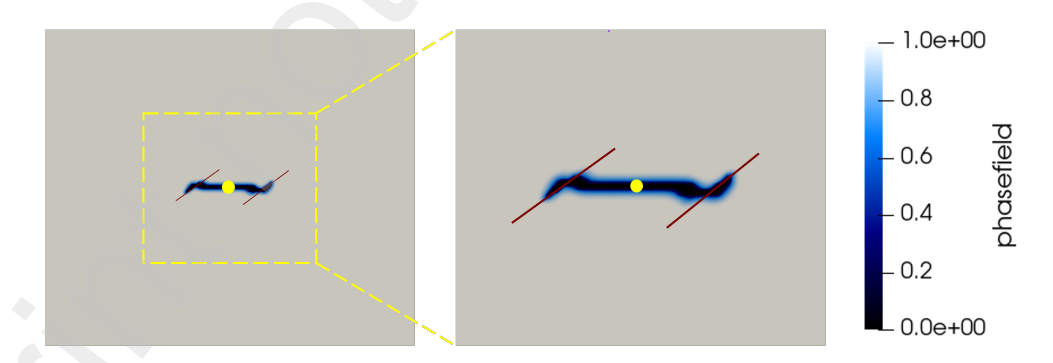


Fig. 16 The fracture interacting with weak interfaces under  $\Delta \sigma = 0$  MPa.

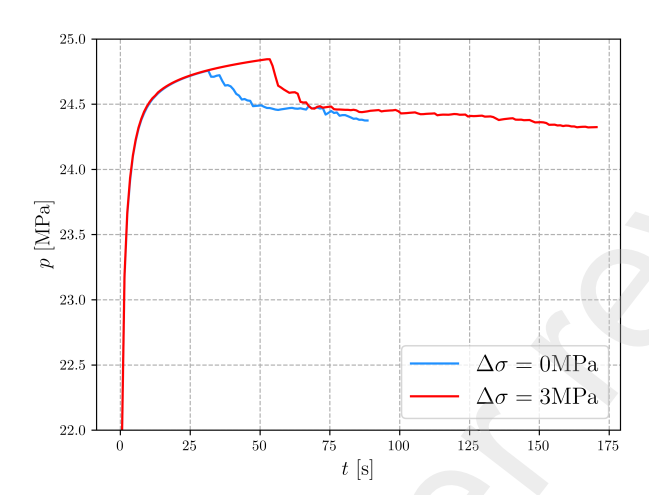


Fig. 17 Pressure response at injection point with weak interfaces in  $CO_2$  fracturing under  $\Delta \sigma = 0$  MPa and 3 MPa.

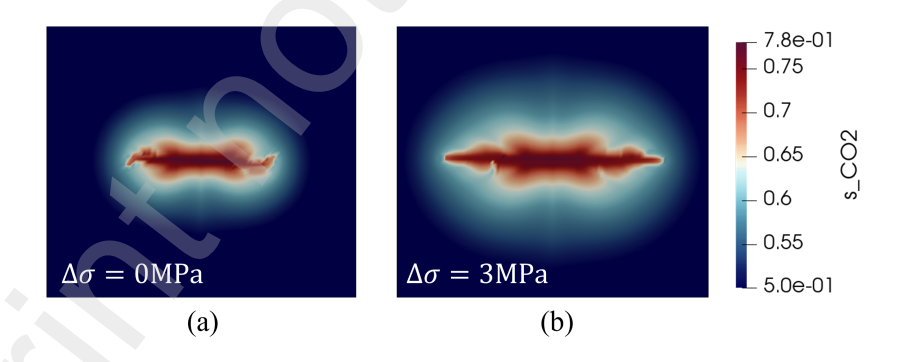


Fig. 18 CO<sub>2</sub> saturation with weak interfaces under  $\Delta \sigma = 0$  MPa and 3 MPa.

of fracture initiation and propagation mechanisms during subsurface CO<sub>2</sub> injection. Our numerical results show that CO<sub>2</sub> injection does not lead to the high pressure build-up or subsequent pressure drop as observed in experimental studies (Song et al., 2019; Liu et al., 2017; Ishida et al., 2021). We also find that the interaction between hydraulic fractures and pre-existing weak interfaces becomes more complex with CO<sub>2</sub> injection. Due to its low viscosity and slow flow rate, CO<sub>2</sub> more readily infiltrates these features, promoting branching and complex fracture geometries. As demonstrated in Section 5.4, in-situ stress differences significantly influence fracture propagation paths. These findings underscore the importance of accurately characterizing the in-situ stress field during early site assessments to improve predictions of fracture behavior in naturally fractured reservoirs.

In this study, weak interfaces are represented by assigning a lower fracture toughness than that of the surrounding rock. However, additional factors may need to be considered. For instance, natural fractures typically exhibit a Biot coefficient close to 1, significantly higher than that of intact rock, which can induce greater tensile stress, as shown analytically in You and Yoshioka (2025). When injecting low-viscosity fluids such as supercritical CO<sub>2</sub>, the pressure front can travel farther, potentially triggering fracture initiation at distant natural fractures, a phenomenon referred to as "remote fracturing" (You and Yoshioka, 2025). Compared to water-based fracturing, remote fracturing is more likely with CO<sub>2</sub> injection due to its ability to reach supercritical conditions under typical subsurface environments. This highlights the importance of monitoring for remote fracturing during field operations involving CO<sub>2</sub>. Another critical factor is the permeability of natural fractures. High-permeability fractures tend to attract the propagating fracture front and dissipate pressure, promoting the formation of complex fracture networks.

A potential future study is to extend the current TH<sup>2</sup>M phase-field model to incorporate other fracturing fluids, such as liquid nitrogen (Yang et al., 2024), liquefied petroleum gas (Gandossi and Von Estorff, 2015), or high-energy gas (Yang et al., 1992). This would likely require the use of fluid-specific equations of state to accurately model two-phase flow behavior. Moreover, these thermally sensitive fluids may undergo phase transitions near the fracture tip, where temperature and pressure can change rapidly. Such conditions can cause complex flow environments in which multiple fluid phases (supercritical, gaseous, and liquid) coexist (Osiptsov, 2017).

## 7. Conclusions

This paper proposes a novel variational phase-field fracture approach that considers non-isothermal  ${\rm CO_2}$ -water two-phase flow in deformable porous media. Building on our previous thermo-hydromechanical (THM) phase-field model, the fluid flow component has been extended to the two-phase case by incorporating capillary effects. Saturation is determined from the capillary pressure relationship. Furthermore, the equivalent liquid pressure is used to represent the pore fluid energy within the total energy functional. A hybrid monolithic-staggered scheme has been implemented to solve the  ${\rm TH^2M}$  phase-field system, incorporating an adapted fixed-stress split method that accounts for thermal stress, within the open-source finite element code OpenGeoSys (Bilke et al., 2023). The proposed model has been verified against analytical solutions for one-dimensional two-phase flow transport (McWhorter problem) and plane-strain hydraulic fracture propagation (KGD problem).

Through numerical experiments, we compared  $CO_2$  fracturing with water-based fracturing to highlight the distinct characteristics of  $CO_2$  injection. The following conclusions can be drawn:

1. Cold CO<sub>2</sub> injection can initiate fracture propagation at a low injection rate, even below the critical pressure.

- 2. A single-phase assumption is inadequate for simulating CO<sub>2</sub> fracturing, as it neglects capillary effects and changes in relative permeability.
- 3. Fracture growth becomes more pronounced with colder CO<sub>2</sub> injection.
- When interacting with weak interfaces, fracture propagation induced by CO<sub>2</sub> tends to develop
  a more complex morphology.

## 417 Declaration of competing interest

The authors declare that they have no known competing financial interests or personal relationships that could have appeared to influence the work reported in this paper.

## 420 Data availability

412

413

414

415 416

418

419

433

434

435

437

No data was used for the research described in the article.

## 422 Acknowledgement

This work is supported by the National Key Research and Development Project (No.2023YFE0110900) and National Natural Science Foundation of China (No.42320104003, 42077247).

# 425 Appendix

# <sup>426</sup> Appendix A. Peng-Robinson equation for the state of CO<sub>2</sub>

Peng-Robinson equation of state (PR-EOS) is a widely used cubic equation of state for describing the behaviour of real gases, particularly hydrocarbons. It accounts for non-ideal behaviour of fluids over a range of temperatures and pressures. The equation is given in terms of the molar density  $\rho$ as:

$$P = \frac{RT\rho}{1 - b\rho} - \frac{a\rho^2}{1 + 2b\rho - b^2\rho^2}$$
 (A.1)

where P is the pressure, T the temperature,  $\rho$  the molar density, R the universal gas constant, and a, b are substance-specific parameters.

The parameters a and b are computed from the critical temperature  $T_c$  in Kelvin, critical pressure  $p_c$  in Pascal, and (dimensionless) acentric factor  $\omega$  as follows:

$$a = 0.457235 \frac{R^2 T_c^2}{p_c} \tag{A.2}$$

$$b = 0.077796 \frac{RT_c}{p_c} \tag{A.3}$$

The Peng-Robinson equation is applicable for a wide range of substances (gases and liquids), particularly hydrocarbons, at conditions ranging from subcritical to supercritical. The EOS is not suitable for solid phases or very low-temperature applications where real gases behave ideally.

## Appendix B. Discretization of TH<sup>2</sup>M phase-field modeling with FEM

The variables  $v, T, p_c, p_{CR}$  and  $\mathbf{u}$  are defined at integration points as nodal values so that the field discretization form for the variables themselves and the respective gradients can be written as

$$\mathbf{u} = \sum_{i=1}^{n} N_{i}^{u} u_{i} = \mathbf{N}_{u} \hat{\mathbf{u}}, \ v = \sum_{i=1}^{n} N_{i}^{v} v_{i} = \mathbf{N}_{v} \hat{\mathbf{v}}, \ p_{c} = \sum_{i=1}^{n} N_{i}^{p} p_{c,i} = \mathbf{N}_{p} \hat{p}_{c}$$

$$p_{CR} = \sum_{i=1}^{n} N_{i}^{p} p_{CR,i} = \mathbf{N}_{p} p_{CR}^{2}, \ T = \sum_{i=1}^{n} N_{i} T_{i} = \mathbf{N}_{T} \hat{T}, \varepsilon = \sum_{i=1}^{n} B_{i}^{u} u_{i} = \mathbf{B}_{u} \hat{\mathbf{u}}$$

$$\nabla v = \sum_{i=1}^{n} B_{i}^{v} v_{i} = \mathbf{B}_{v} \hat{\mathbf{v}}, \ \nabla p_{c} = \sum_{i=1}^{n} B_{i}^{p} p_{c,i} = \mathbf{B}_{p} \hat{p}_{c}, \ \nabla p_{CR} = \sum_{i=1}^{n} B_{i}^{p} p_{CR,i} = \mathbf{B}_{p} p_{CR}^{2}$$

$$\nabla T = \sum_{i=1}^{n} B_{i}^{T} T_{i} = \mathbf{B}_{T} \hat{T}$$

$$(B.1)$$

where  $\hat{T}$ ,  $\hat{p_c}$ ,  $\hat{p_c}$ ,  $\hat{\mathbf{u}}$  and  $\hat{v}$  represent the vectors of the integration point values in one element.

Note that  $\varepsilon$  is a vector of independent strain variables but not a tensor, e.g.,  $\varepsilon = \left[\varepsilon_{xx}, \, \varepsilon_{yy}, \, \varepsilon_{xy}\right]^T$  in

2D problem. Shape functions  $N_u$ ,  $N_T$ ,  $N_{p_c}$ ,  $N_{p_{CR}}$  and  $N_v$  are represented as matrixes for vector field  $\mathbf{u}$  and a vector for scalar field like p, v and T and they are also used as test functions for each process:

$$\begin{cases}
\mathbf{N}_{u} = \begin{bmatrix} N_{1}^{u} & 0 & \dots & N_{i}^{u} & 0 & \dots & N_{n}^{u} & 0 \\ 0 & N_{1}^{u} & \dots & 0 & N_{i}^{u} & \dots & 0 & N_{n}^{u} \end{bmatrix} \\
\mathbf{N}_{T} = \begin{bmatrix} N_{1}^{T} & \dots & N_{i}^{T} & \dots & N_{n}^{T} \end{bmatrix} \\
\mathbf{N}_{p_{c}} = \begin{bmatrix} N_{1}^{p_{c}} & \dots & N_{i}^{p_{c}} & \dots & N_{n}^{p_{c}} \end{bmatrix} \\
\mathbf{N}_{p_{CR}} = \begin{bmatrix} N_{1}^{p_{CR}} & \dots & N_{i}^{p_{CR}} & \dots & N_{n}^{p_{CR}} \end{bmatrix} \\
\mathbf{N}_{v} = \begin{bmatrix} N_{1}^{v} & \dots & N_{i}^{v} & \dots & N_{n}^{v} \end{bmatrix}
\end{cases}$$
(B.2)

The Galerkin finite element method considers the same shape functions in the present work, i.e.,  $N_i^u = N_i^T = N_i^{p_c} = N_i^{p_{CR}} = N_i^v.$ 

449

$$\{T\}_m = \{T\}_{m-1} - [K^{TT}]_{m-1}^{-1} \{r^T\}_{m-1},$$
 (B.3)

$$\left\{\begin{array}{c} \mathbf{p_{CR}} \\ \mathbf{p_{c}} \end{array}\right\}_{m} = \left\{\begin{array}{c} \mathbf{p_{CR}} \\ \mathbf{p_{c}} \end{array}\right\}_{m-1} - \left[\begin{array}{cc} \mathbf{K}^{C\mathbf{p_{CR}}} & \mathbf{K}^{C\mathbf{p_{c}}} \\ \mathbf{K}^{C\mathbf{p_{CR}}} & \mathbf{K}^{W\mathbf{p_{c}}} \end{array}\right]_{m-1}^{-1} \left\{\begin{array}{c} \mathbf{r}^{C} \\ \mathbf{r}^{W} \end{array}\right\}_{m-1},$$
(B.4)

$$\left\{ \begin{array}{c} \mathbf{u} \\ \mathbf{v} \end{array} \right\}_{m} = \left\{ \begin{array}{c} \mathbf{u} \\ \mathbf{v} \end{array} \right\}_{m-1} - \left[ \begin{array}{cc} \mathbf{K}^{\mathbf{u}\mathbf{u}} & 0 \\ 0 & \mathbf{K}^{vv} \end{array} \right]_{m-1}^{-1} \left\{ \begin{array}{c} \mathbf{r}^{\mathbf{u}} \\ \mathbf{r}^{v} \end{array} \right\}_{m-1}.$$
 (B.5)

The residuals of each field are given as

$$\boldsymbol{r}_{m}^{T} = \int_{\Omega} 3\beta K_{\text{eff}} \boldsymbol{N}_{T}^{T} \boldsymbol{N}_{T} \hat{T}^{k,m} \frac{\varepsilon_{v}(\hat{\boldsymbol{u}}^{k,m-1}) - \varepsilon_{v}(\hat{\boldsymbol{u}}^{k-1})}{\Delta t} dV$$

$$+ \int_{\Omega} \boldsymbol{N}_{T}^{T} \boldsymbol{N}_{T} (\rho c)_{m} \frac{\hat{T}^{k,m} - \hat{T}^{k-1}}{\Delta t} dV - \int_{\Omega} \boldsymbol{B}_{T}^{T} \boldsymbol{N}_{T} \rho_{LR} c_{p,L} \hat{\mathbf{q}}_{L}^{k,m-1} T^{k,m} dV$$

$$- \int_{\Omega} \boldsymbol{B}_{T}^{T} \boldsymbol{N}_{T} \rho_{CR} c_{p,C} \hat{\mathbf{q}}_{C}^{k,m-1} T^{k,m} dV + \int_{\Omega} \boldsymbol{B}_{T}^{T} \boldsymbol{B}_{T} \boldsymbol{\lambda}_{\text{eff}} \hat{T}^{k,m} dV$$

$$- \int_{\Omega} \boldsymbol{N}_{T}^{T} Q_{T} dV + \int_{\partial_{N} \Omega} \boldsymbol{N}_{T}^{T} \mathbf{q}_{Tn} dS$$

$$(B.6)$$

$$\begin{split} & \boldsymbol{r}_{m}^{W} = \int_{\Omega} \alpha S_{L}^{k,m-1} \rho_{LR} \boldsymbol{N}_{p}^{T} \frac{\varepsilon_{v}(\hat{\boldsymbol{u}}^{k,m-1}) - \varepsilon_{v}(\hat{\boldsymbol{u}}^{k-1})}{\Delta t} dV + \int_{\Omega} S_{L}^{k,m-1} \rho_{LR} \boldsymbol{N}_{p}^{T} \frac{1}{M_{p}} \boldsymbol{N}_{p} \frac{\hat{p}_{CR}^{k,m} - \hat{p}_{CR}^{k-1}}{\Delta t} dV \\ & - \int_{\Omega} S_{L}^{k,m-1} \rho_{LR} \boldsymbol{N}_{p}^{T} \frac{1}{M_{T}} \boldsymbol{N}_{T} \frac{\hat{T}^{k,m-} - \hat{T}^{k-1}}{\Delta t} dV + \int_{\Omega} \rho_{LR} \boldsymbol{B}_{p}^{T} \frac{k_{L}^{\text{rel}} \mathbf{k}_{s}}{\mu_{LR}} \boldsymbol{B}_{p} dV (\hat{p}_{CR}^{k,m} - \hat{p}_{c}^{k,m} - \boldsymbol{b}) \\ & + \int_{\Omega} \phi S_{L}^{k,m-1} \boldsymbol{N}_{p}^{T} \frac{\rho_{LR}^{k,m} - \rho_{LR}^{k-1}}{\Delta t} dV + \int_{\Omega} \frac{\alpha^{2}}{K} S_{L}^{k,m-1} \rho_{LR} \boldsymbol{N}_{p}^{T} \boldsymbol{N}_{p} dV \frac{\hat{p}_{FR}^{k,m} - \hat{p}_{FR}^{k,m-1}}{\Delta t} \\ & + \int_{\Omega} \phi \rho_{LR} \boldsymbol{N}_{p}^{T} \frac{S_{L}^{k,m-1} - S_{L}^{k-1}}{\Delta t} dV - \int_{\Omega} \boldsymbol{N}_{p}^{T} S_{L}^{k,m-1} \rho_{LR} p_{c} \frac{1}{M_{p}} \frac{S_{L}^{k,m-1} - S_{L}^{k-1}}{\Delta t} dV \\ & - \int_{\Omega} S_{L}^{k,m-1} \boldsymbol{N}_{p}^{T} \boldsymbol{N}_{p} \rho_{LR} \frac{1}{M_{p}} \frac{\hat{p}_{c}^{k,m} - \hat{p}_{c}^{k-1}}{\Delta t} S_{L}^{k,m-1} dV + \int_{\Omega} 3\alpha \alpha_{s} S_{L}^{k,m-1} \rho_{LR} \boldsymbol{N}_{p}^{T} \boldsymbol{N}_{T} \frac{\hat{T}^{k,m} - \hat{T}^{k,m-1}}{\Delta t} dV \\ & - \int_{\Omega} \boldsymbol{N}_{p}^{T} Q_{L} dV + \int_{\partial_{N} \Omega} \boldsymbol{N}_{p}^{T} q_{n} dS \end{split}$$

$$\begin{split} r_{m}^{C} &= \int_{\Omega} \alpha S_{C}^{k,m-1} \rho_{CR} N_{p}^{T} \frac{\varepsilon_{v}(\hat{\boldsymbol{u}}^{k,m-1}) - \varepsilon_{v}(\hat{\boldsymbol{u}}^{k-1})}{\Delta t} dV + \int_{\Omega} S_{C}^{k,m-1} \rho_{CR} N_{p}^{T} \frac{1}{M_{p}} N_{p} \frac{\hat{p}_{CR}^{k,m} - \hat{p}_{CR}^{k-1}}{\Delta t} dV \\ &\quad (B.8) \end{split}$$

$$- \int_{\Omega} S_{C}^{k,m-1} \rho_{CR} N_{p}^{T} \frac{1}{M_{T}} N_{T} \frac{\hat{T}^{k,m-} - \hat{T}^{k-1}}{\Delta t} dV + \int_{\Omega} \rho_{CR} B_{p}^{T} \frac{k_{C}^{\text{rel}} \mathbf{k}_{s}}{\mu_{CR}} B_{p} dV (\hat{p}_{CR}^{k,m} - \mathbf{b}) \\ + \int_{\Omega} \phi S_{C}^{k,m-1} N_{p}^{T} \frac{\rho_{CR}^{k,m} - \rho_{CR}^{k-1}}{\Delta t} dV + \int_{\Omega} \frac{\alpha^{2}}{K} S_{C}^{k,m-1} \rho_{CR} N_{p}^{T} N_{p} dV \frac{\hat{p}_{FR}^{k,m} - \hat{p}_{FR}^{k,m-1}}{\Delta t} \\ - \int_{\Omega} \phi \rho_{CR} N_{p}^{T} \frac{S_{L}^{k,m-1} - S_{L}^{k-1}}{\Delta t} dV - \int_{\Omega} N_{p}^{T} S_{C}^{k,m-1} \rho_{CR} p_{c} \frac{1}{M_{p}} \frac{S_{L}^{k,m-1} - S_{L}^{k-1}}{\Delta t} dV \\ - \int_{\Omega} S_{C}^{k,m-1} N_{p}^{T} N_{p} \rho_{CR} \frac{1}{M_{p}} \frac{\hat{p}_{C}^{k,m} - \hat{p}_{C}^{k-1}}{\Delta t} S_{L}^{k,m-1} dV + \int_{\Omega} 3\alpha \alpha_{s} S_{C}^{k,m-1} \rho_{CR} N_{p}^{T} N_{T} \frac{\hat{T}^{k,m} - \hat{T}^{k,m-1}}{\Delta t} dV \\ - \int_{\Omega} N_{p}^{T} Q_{C} dV + \int_{\partial_{N} \Omega} N_{p}^{T} q_{n} dS \end{split}$$

$$\boldsymbol{r}_{m}^{\boldsymbol{u}} = \int_{\Omega} g(v) \boldsymbol{B}_{u}^{T} \boldsymbol{\sigma}_{e}^{k,m} dV - \int_{\Omega} \boldsymbol{B}_{u}^{T} \alpha(v) \boldsymbol{N}_{p} \hat{p}_{FR}^{k,m} \boldsymbol{I} dV$$

$$- \int_{\Omega} \boldsymbol{N}_{\mathbf{u}}^{T} \bar{\mathbf{t}} dS$$
(B.

$$\boldsymbol{r}_{m}^{v} = \int_{\Omega} 2(1-k)\boldsymbol{N}_{v}^{T}\boldsymbol{N}_{v}\psi_{+}(\mathbf{u})^{k,m-1}dV\hat{v} + \frac{G_{c}}{4c_{n}}\int_{\Omega} \left[-\frac{n}{\ell}(1-\boldsymbol{N}_{v}\hat{v})^{n-1}\boldsymbol{N}_{v}^{T} + 2\ell\boldsymbol{B}_{v}^{T}\boldsymbol{B}_{v}\hat{v}\right]dV$$

$$+ \int_{\Omega} 2(1-k)\boldsymbol{N}_{v}^{T}\frac{\boldsymbol{N}_{p}\hat{p}_{FR}}{2}H(Tr(\varepsilon_{e}))(1-\alpha_{m})dV\hat{v}$$
(B.10)

and the Jacobian matrices for each field are given as

$$K^{TT} = \frac{\partial \boldsymbol{r}^{T}}{\partial \hat{T}} = \int_{\Omega} 3\beta K_{\text{eff}} \boldsymbol{N}_{T}^{T} \boldsymbol{N}_{T} \frac{\varepsilon_{v}(\hat{\boldsymbol{u}}^{k,m-1}) - \varepsilon_{v}(\hat{\boldsymbol{u}}^{k-1})}{\Delta t} dV$$

$$+ \int_{\Omega} \boldsymbol{N}_{T}^{T} \boldsymbol{N}_{T} (\rho c)_{m} \frac{1}{\Delta t} dV + \int_{\Omega} \boldsymbol{B}_{T}^{T} \boldsymbol{\lambda}_{\text{eff}} \boldsymbol{B}_{T} dV$$

$$- \int_{\Omega} \boldsymbol{B}_{T}^{T} \boldsymbol{N}_{T} \rho_{LR} c_{p,L} \hat{\mathbf{q}}_{L}^{k,m-1} dV - \int_{\Omega} \boldsymbol{B}_{T}^{T} \boldsymbol{N}_{T} \rho_{CR} c_{p,C} \hat{\mathbf{q}}_{C}^{k,m-1} dV$$
(B.11)

$$\boldsymbol{K}^{Wp_c} = \frac{\partial \boldsymbol{r}^W}{\partial \hat{p}_c} = -\int_{\Omega} \rho_{LR} \boldsymbol{B}_p^T \frac{k_L^{\text{rel}} \mathbf{k}_s}{\mu_{LR}} \boldsymbol{B}_p dV 
-\int_{\Omega} \frac{\alpha^2}{K} S_L^{k,m-1} \rho_{LR} \boldsymbol{N}_p^T \boldsymbol{N}_p dV \frac{1}{\Delta t} - \int_{\Omega} \phi S_L^{k,m-1} \rho_{LR} c_{f,L} \boldsymbol{N}_p^T \boldsymbol{N}_p \frac{1}{\Delta t} dV 
-\int_{\Omega} \boldsymbol{N}_p^T \boldsymbol{N}_p S_L^{k,m-1} \rho_{LR} \frac{1}{M_p} \frac{S_L^{k,m-1} - S_L^{k-1}}{\Delta t} dV - \int_{\Omega} S_L^{k,m-1} \boldsymbol{N}_p^T \boldsymbol{N}_p \rho_{LR} \frac{1}{M_p} \frac{1}{\Delta t} S_L^{k,m-1} dV$$
(B.12)

$$\boldsymbol{K}^{Wp_c} = \frac{\partial \boldsymbol{r}^W}{\partial \hat{p}_c} = -\boldsymbol{M}_{pc}^W - \boldsymbol{L}_{pc}^W + \boldsymbol{A}_{pc}^W + \boldsymbol{S}_{pc}^W + \boldsymbol{D}_{pc}^W - \boldsymbol{F}_{pc}^W$$
(B.13)

$$\boldsymbol{K}^{Wp_{CR}} = \frac{\partial \boldsymbol{r}^W}{\partial \hat{p}_{CR}} = \boldsymbol{M}_{pCR}^W + \boldsymbol{L}_{pCR}^W + \boldsymbol{A}_{pCR}^W + \boldsymbol{S}_{pCR}^W + \boldsymbol{D}_{pCR}^W + \boldsymbol{F}_{pCR}^W$$
(B.14)

$$\boldsymbol{K}^{Cp_c} = \frac{\partial \boldsymbol{r}^C}{\partial \hat{p}_c} = -\boldsymbol{M}_{pc}^C + \boldsymbol{L}_{pc}^C + \boldsymbol{A}_{pc}^C - \boldsymbol{S}_{pc}^C + \boldsymbol{D}_{pc}^C - \boldsymbol{F}_{pc}^C$$
(B.15)

$$\boldsymbol{K}^{Cp_{CR}} = \frac{\partial \boldsymbol{r}^{C}}{\partial \hat{n}_{CR}} = \boldsymbol{M}_{pCR}^{C} + \boldsymbol{L}_{pCR}^{C} + \boldsymbol{A}_{pCR}^{C} - \boldsymbol{S}_{pCR}^{C} + \boldsymbol{D}_{pCR}^{C} + \boldsymbol{F}_{pCR}^{C}$$
(B.16)

$$K^{uu} = \frac{\partial r^{u}}{\partial \hat{u}} = \int_{\Omega} g(v) B_{u}^{T} \mathbb{C}_{+} B_{u} dV$$
(B.17)

$$\boldsymbol{K}^{vv} = \frac{\partial \boldsymbol{r}^{v}}{\partial \hat{v}} = \int_{\Omega} 2(1-k)\psi_{+}(\mathbf{u})^{k,m-1}\boldsymbol{N}_{v}^{T}\boldsymbol{N}_{v}dV$$

$$+ \int_{\Omega} 2(1-k)\boldsymbol{N}_{v}^{T}\frac{\boldsymbol{N}_{p}\hat{p}_{FR}}{2}H(\operatorname{Tr}(\varepsilon_{e}))(1-\alpha_{m})dV$$

$$+ \frac{G_{c}}{4c_{n}}\int_{\Omega} \left[\frac{n(n-1)}{\ell}(1-\boldsymbol{N}_{v}\hat{v})^{n-2}\boldsymbol{N}_{v}^{T}\boldsymbol{N}_{v} + 2\ell\boldsymbol{B}_{v}^{T}\boldsymbol{B}_{v}\right]dV$$
(B.18)

$$\boldsymbol{M}_{pc}^{W} = \int_{\Omega} S_{L}^{k,m-1} \boldsymbol{N}_{p}^{T} \boldsymbol{N}_{p} \rho_{LR} \frac{1}{M_{p}} \frac{1}{\Delta t} S_{L}^{k,m-1} dV$$
(B.19)

$$\boldsymbol{M}_{pCR}^{W} = \int_{\Omega} S_{L}^{k,m-1} \rho_{LR} \boldsymbol{N}_{p}^{T} \frac{1}{M_{p}} \boldsymbol{N}_{p} \frac{1}{\Delta t} dV$$
(B.20)

$$\boldsymbol{M}_{pc}^{C} = \int_{\Omega} S_{C}^{k,m-1} \boldsymbol{N}_{p}^{T} \boldsymbol{N}_{p} \rho_{CR} \frac{1}{M_{p}} \frac{1}{\Delta t} S_{L}^{k,m-1} dV$$
(B.21)

$$\boldsymbol{M}_{pCR}^{C} = \int_{\Omega} S_{C}^{k,m-1} \rho_{CR} \boldsymbol{N}_{p}^{T} \frac{1}{M_{p}} \boldsymbol{N}_{p} \frac{1}{\Delta t} dV$$
(B.22)

$$\boldsymbol{L}_{pc}^{W} = \boldsymbol{L}_{pCR}^{W} = \int_{\Omega} \rho_{LR} \boldsymbol{B}_{p}^{T} \frac{k_{L}^{\text{rel}} \mathbf{k}_{s}}{\mu_{LR}} \boldsymbol{B}_{p} dV$$
(B.23)

$$\boldsymbol{L}_{pc}^{C} = 0 \tag{B.24}$$

$$\boldsymbol{L}_{pCR}^{C} = \int_{\Omega} \rho_{CR} \boldsymbol{B}_{p}^{T} \frac{k_{C}^{\text{rel}} \boldsymbol{\mathbf{k}}_{s}}{\mu_{CR}} \boldsymbol{B}_{p} dV$$
 (B.25)

$$\boldsymbol{A}_{pc}^{W} = \int_{\Omega} \boldsymbol{B}_{p}^{T} \left( \frac{\partial \rho_{LR}}{\partial p_{c}} \frac{k_{L}^{\text{rel}} \mathbf{k}_{s}}{\mu_{LR}} + \rho_{LR} \frac{k_{L}^{\text{rel}}}{\partial p_{c}} \frac{\mathbf{k}_{s}}{\mu_{LR}} \right) \boldsymbol{B}_{p} \left( \hat{p}_{CR}^{k,m} - \hat{p}_{c}^{k,m} \right) \boldsymbol{N}_{p} dV$$
(B.26)

$$\boldsymbol{A}_{pCR}^{W} = \int_{\Omega} \boldsymbol{B}_{p}^{T} \left( \frac{\partial \rho_{LR}}{\partial p_{CR}} \frac{k_{L}^{\text{rel}} \mathbf{k}_{s}}{\mu_{LR}} \right) \boldsymbol{B}_{p} \left( \hat{p}_{CR}^{k,m} - \hat{p}_{c}^{k,m} \right) \boldsymbol{N}_{p} dV$$
(B.27)

$$\boldsymbol{A}_{pc}^{C} = \int_{\Omega} \boldsymbol{B}_{p}^{T} \left( \rho_{CR} \frac{k_{C}^{\text{rel}}}{\partial p_{c}} \frac{\mathbf{k}_{s}}{\mu_{CR}} \right) \boldsymbol{B}_{p} \hat{p}_{CR}^{k,m} \boldsymbol{N}_{p} dV$$
(B.28)

$$\boldsymbol{A}_{pCR}^{C} = \int_{\Omega} \boldsymbol{B}_{p}^{T} \left( \frac{\partial \rho_{CR}}{\partial p_{CR}} \frac{k_{C}^{\text{rel}} \mathbf{k}_{s}}{\mu_{CR}} \right) \boldsymbol{B}_{p} \hat{p}_{CR}^{k,m} \boldsymbol{N}_{p} dV$$
(B.29)

$$S_{pc}^{W} = \int_{\Omega} \mathbf{N}_{p}^{T} \left( \left( \phi \frac{\partial \rho_{LR}}{\partial p_{c}} - \left( \frac{\partial S_{L}^{k,m-1}}{\partial p_{c}} \rho_{LR} + S_{L}^{k,m-1} \frac{\partial \rho_{LR}}{\partial p_{c}} \right) p_{c} \frac{1}{M_{p}} \right) - S_{L}^{k,m-1} \rho_{LR} \frac{1}{M_{p}} \left( \frac{1}{M_{p}} \right) \frac{S_{L}^{k,m-1} - S_{L}^{k-1}}{\Delta t} + \left( \phi \rho_{LR} - S_{L}^{k,m-1} \rho_{LR} p_{c} \frac{1}{M_{p}} \right) \frac{\partial S_{L}^{k,m-1}}{\partial p_{c}} \frac{1}{\Delta t} \right) \mathbf{N}_{p} dV$$
(B.30)

$$\boldsymbol{S}_{pCR}^{W} = \int_{\Omega} \boldsymbol{N}_{p}^{T} \left(\phi \frac{\partial \rho_{LR}}{\partial p_{CR}} - S_{L}^{k,m-1} \frac{\partial \rho_{LR}}{\partial p_{CR}} p_{c} \frac{1}{M_{p}}\right) \frac{S_{L}^{k,m-1} - S_{L}^{k-1}}{\Delta t} \boldsymbol{N}_{p} dV$$
(B.31)

$$\begin{split} \boldsymbol{S}_{pc}^{C} &= \int_{\Omega} \boldsymbol{N}_{p}^{T} ((\phi \frac{\partial \rho_{CR}}{\partial p_{c}} + \left( \frac{\partial S_{C}^{k,m-1}}{\partial p_{c}} \rho_{CR} + S_{C}^{k,m-1} \frac{\partial \rho_{CR}}{\partial p_{c}} \right) p_{c} \frac{1}{M_{p}} \\ &+ S_{C}^{k,m-1} \rho_{CR} \frac{1}{M_{p}}) \frac{S_{L}^{k,m-1} - S_{L}^{k-1}}{\Delta t} + (\phi \rho_{CR} + S_{C}^{k,m-1} \rho_{CR} p_{c} \frac{1}{M_{p}}) \frac{\partial S_{L}^{k,m-1}}{\partial p_{c}} \frac{1}{\Delta t}) \boldsymbol{N}_{p} \, dV \end{split} \tag{B.32}$$

$$\boldsymbol{S}_{pCR}^{C} = \int_{\Omega} \boldsymbol{N}_{p}^{T} \left( \left( \phi \frac{\partial \rho_{CR}}{\partial p_{CR}} + S_{C}^{k,m-1} \frac{\partial \rho_{CR}}{\partial p_{CR}} p_{c} \frac{1}{M_{p}} \right) \frac{S_{L}^{k,m-1} - S_{L}^{k-1}}{\Delta t} \right) \boldsymbol{N}_{p} \, dV \tag{B.33}$$

$$\boldsymbol{D}_{pc}^{W} = \int_{\Omega} \phi \boldsymbol{N}_{p}^{T} \left( \frac{\partial S_{L}^{k,m-1}}{\partial p_{c}} \frac{\rho_{LR}^{k,m} - \rho_{LR}^{k-1}}{\Delta t} + S_{L}^{k,m-1} \frac{\partial \rho_{LR}^{k,m}}{\partial p_{c}} \frac{1}{\Delta t} \right) \boldsymbol{N}_{p} \, dV$$
 (B.34)

$$\boldsymbol{D}_{pCR}^{W} = \int_{\Omega} \phi S_{L}^{k,m-1} \boldsymbol{N}_{p}^{T} \frac{\partial \rho_{LR}^{k,m}}{\partial p_{CR}} \frac{1}{\Delta t} \boldsymbol{N}_{p} \, dV$$
(B.35)

$$\boldsymbol{D}_{pc}^{C} = \int_{\Omega} \phi \boldsymbol{N}_{p}^{T} \left( \frac{\partial S_{C}^{k,m-1}}{\partial p_{c}} \frac{\rho_{CR}^{k,m} - \rho_{CR}^{k-1}}{\Delta t} + S_{C}^{k,m-1} \frac{\partial \rho_{CR}^{k,m}}{\partial p_{c}} \frac{1}{\Delta t} \right) \boldsymbol{N}_{p} \, dV$$
 (B.36)

$$\boldsymbol{D}_{pCR}^{C} = \int_{\Omega} \phi S_{C}^{k,m-1} \boldsymbol{N}_{p}^{T} \frac{\partial \rho_{CR}^{k,m}}{\partial p_{CR}} \frac{1}{\Delta t} \boldsymbol{N}_{p} \, dV$$
(B.37)

$$\boldsymbol{F}_{pc}^{W} = \int_{\Omega} S_{L}^{k,m-1} \rho_{LR} \frac{\alpha^{2}}{K} \boldsymbol{N}_{p}^{T} \boldsymbol{N}_{p} S_{L}^{k,m-1} dV \frac{1}{\Delta t}$$
(B.38)

$$\boldsymbol{F}_{pCR}^{W} = \int_{\Omega} S_{L}^{k,m-1} \rho_{LR} \frac{\alpha^{2}}{K} \boldsymbol{N}_{p}^{T} \boldsymbol{N}_{p} dV \frac{1}{\Delta t}$$
(B.39)

$$\boldsymbol{F}_{pc}^{C} = \int_{C} S_{C}^{k,m-1} \rho_{LR} \frac{\alpha^{2}}{K} \boldsymbol{N}_{p}^{T} \boldsymbol{N}_{p} S_{L}^{k,m-1} dV \frac{1}{\Delta t}$$
(B.40)

$$\boldsymbol{F}_{pCR}^{C} = \int_{C} S_{C}^{k,m-1} \rho_{LR} \frac{\alpha^{2}}{K} \boldsymbol{N}_{p}^{T} \boldsymbol{N}_{p} dV \frac{1}{\Delta t}$$
(B.41)

## 487 References

- Adachi, J., Siebrits, E, m., Peirce, A., Desroches, J., 2007. Computer simulation of hydraulic fractures. International Journal of Rock Mechanics and Mining Sciences 44, 739–757.
- Afanasyev, A.A., 2013. Multiphase compositional modelling of co2 injection under subcritical conditions: the impact of dissolution and phase transitions between liquid and gaseous co2 on reservoir temperature. International Journal of Greenhouse Gas Control 19, 731–742.
- Amor, H., Marigo, J.J., Maurini, C., 2009. Regularized formulation of the variational brittle fracture with unilateral contact: Numerical experiments. Journal of the Mechanics and Physics of Solids 57, 1209–1229.
- Bai, M., Zhang, Z., Fu, X., 2016. A review on well integrity issues for co2 geological storage and enhanced gas recovery. Renewable and Sustainable Energy Reviews 59, 920–926.
- Basu, D., Misra, A., Puppala, A.J., 2015. Sustainability and geotechnical engineering: perspectives and review. Canadian geotechnical journal 52, 96–113.
- Bilke, L., Lehmann, C., Naumov, D., Fischer, T., Wang, W., Buchwald, J., Rink, K., Grunwald,
   N., Zill, F., Kiszkurno, F.K., Mollali, M., Nagel, T., Thiedau, J., Gerasimov, T., Ziaei Rad, V.,
- Kurgyis, K., Lu, R., Silbermann, C., Heinze, J., Vehling, F., Meng, B., Yoshioka, K., You, T.,
- <sup>503</sup> Chaudhry, A., Shao, H., Günther, L., Kantzenbach, M., Kolditz, O., Meisel, T., 2023. Open-<sup>504</sup> geosys. URL: https://doi.org/10.5281/zenodo.7716938, doi:10.5281/zenodo.7716938.
- Bourdin, B., Chukwudozie, C., Yoshioka, K., 2012. A variational approach to the numerical simulation of hydraulic fracturing, in: SPE annual technical conference and exhibition?, SPE. pp. SPE-159154.
- Bourdin, B., Francfort, G.A., Marigo, J.J., 2000. Numerical experiments in revisited brittle fracture.
   Journal of the Mechanics and Physics of Solids 48, 797–826.
- Bourdin, B., Francfort, G.A., Marigo, J.J., 2008. The variational approach to fracture. Journal of elasticity 91, 5–148.

- 512 Brooks, R.H., 1965. Hydraulic properties of porous media. Colorado State University.
- 513 Brown, H.W., 1951. Capillary pressure investigations. Journal of Petroleum Technology 3, 67–74.
- Cajuhi, T., Sanavia, L., De Lorenzis, L., 2018. Phase-field modeling of fracture in variably saturated
   porous media. Computational Mechanics 61, 299–318.
- Chen, H., Carter, K.E., 2016. Water usage for natural gas production through hydraulic fracturing
   in the united states from 2008 to 2014. Journal of environmental management 170, 152–159.
- Chen, Z., Yang, Z., Wang, M., 2018. Hydro-mechanical coupled mechanisms of hydraulic fracture propagation in rocks with cemented natural fractures. Journal of Petroleum Science and Engineering 163, 421–434.
- Chukwudozie, C., Bourdin, B., Yoshioka, K., 2013. A variational approach to the modeling and numerical simulation of hydraulic fracturing under in-situ stresses, in: Proceedings of the 38th Workshop on Geothermal Reservoir Engineering, Stanford Geothermal Program Stanford, Calif.
- Dai, Y., Hou, B., Lee, S., Wick, T., 2024. A thermal-hydraulic-mechanical-chemical coupling model for acid fracture propagation based on a phase-field method. Rock Mechanics and Rock Engineering 57, 4583–4605.
- Detournay, E., Garagash, D., 2003. The near-tip region of a fluid-driven fracture propagating in a permeable elastic solid. Journal of Fluid Mechanics 494, 1–32.
- Espinoza, D.N., Santamarina, J.C., 2010. Water-co2-mineral systems: Interfacial tension, contact angle, and diffusion—implications to co2 geological storage. Water resources research 46.
- Feng, Y., Firoozabadi, A., 2023. Phase-field simulation of hydraulic fracturing by co2 and water with consideration of thermoporoelasticity. Rock Mechanics and Rock Engineering 56, 7333–7355.
- Feng, Y., Haugen, K., Firoozabadi, A., 2021. Phase-field simulation of hydraulic fracturing by co2, water and nitrogen in 2d and comparison with laboratory data. Journal of Geophysical Research: Solid Earth 126, e2021JB022509.
- Freddi, F., Royer-Carfagni, G., 2010. Regularized variational theories of fracture: a unified approach. Journal of the Mechanics and Physics of Solids 58, 1154–1174.
- Gandossi, L., Von Estorff, U., 2015. An overview of hydraulic fracturing and other formation stimulation technologies for shale gas production. Publications Office of the European Union Luxembourg.
- Gao, J., Wang, H., Sharma, M., 2024. Research progress and prospects of co2 fracturing for
   developing unconventional energy sources. Geoenergy Science and Engineering, 213137.
- Garagash, D.I., 2006. Plane-strain propagation of a fluid-driven fracture during injection and shutin: Asymptotics of large toughness. Engineering fracture mechanics 73, 456–481.
- Grunwald, N., Lehmann, C., Maßmann, J., Naumov, D., Kolditz, O., Nagel, T., 2022. Non-isothermal two-phase flow in deformable porous media: systematic open-source implementation and verification procedure. Geomechanics and Geophysics for Geo-Energy and Geo-Resources 8, 107.

- Guo, T., Zhang, Y., Shen, L., Liu, X., Duan, W., Liao, H., Chen, M., Liu, X., 2022. Numerical study on the law of fracture propagation in supercritical carbon dioxide fracturing. Journal of Petroleum Science and Engineering 208, 109369.
- Heider, Y., Sun, W., 2020. A phase field framework for capillary-induced fracture in unsaturated porous media: Drying-induced vs. hydraulic cracking. Computer Methods in Applied Mechanics and Engineering 359, 112647.
- Ishida, T., Chen, Y., Bennour, Z., Yamashita, H., Inui, S., Nagaya, Y., Naoi, M., Chen, Q.,
   Nakayama, Y., Nagano, Y., 2016. Features of CO<sub>2</sub> fracturing deduced from acoustic emission
   and microscopy in laboratory experiments. Journal of Geophysical Research: Solid Earth 121,
   8080–8098.
- Ishida, T., Desaki, S., Kishimoto, Y., Naoi, M., Fujii, H., 2021. Acoustic emission monitoring of
   hydraulic fracturing using carbon dioxide in a small-scale field experiment. International Journal
   of Rock Mechanics and Mining Sciences 141, 104712.
- Jiang, C., Jing, C., Wang, H., Wang, L., Zhang, L., 2025. Phase-field simulation of co2 fracturing
   crack propagation in thermo-poroelastic media. International Journal of Rock Mechanics and
   Mining Sciences 187, 106052.
- Jiang, Y., Qin, C., Kang, Z., Zhou, J., Li, Y., Liu, H., Song, X., 2018. Experimental study of supercritical co2 fracturing on initiation pressure and fracture propagation in shale under different triaxial stress conditions. Journal of Natural Gas Science and Engineering 55, 382–394.
- Jiao, K., Han, D., Wang, D., Chen, Y., Li, J., Gong, L., Bai, B., Yu, B., 2022. Investigation of
   thermal-hydro-mechanical coupled fracture propagation considering rock damage. Computational
   Geosciences 26, 1167–1187.
- Kim, J., Tchelepi, H.A., Juanes, R., 2011. Stability and convergence of sequential methods for coupled flow and geomechanics: Fixed-stress and fixed-strain splits. Computer Methods in Applied
   Mechanics and Engineering 200, 1591–1606.
- Lee, S., von Wahl, H., Wick, T., 2025a. A thermo-flow-mechanics-fracture model coupling a phasefield interface approach and thermo-fluid-structure interaction. International Journal for Numerical Methods in Engineering 126, e7646.
- Lee, S., Wheeler, M.F., Wick, T., 2025b. A phase-field diffraction model for thermo-hydromechanical propagating fractures. International Journal of Heat and Mass Transfer 239, 126487.
- Li, P., Li, D., Wang, Q., Zhou, K., 2021. Phase-field modeling of hydro-thermally induced fracture in thermo-poroelastic media. Engineering Fracture Mechanics 254, 107887.
- Liu, B., Suzuki, A., Ito, T., 2020. Numerical analysis of different fracturing mechanisms between supercritical co2 and water-based fracturing fluids. International Journal of Rock Mechanics and Mining Sciences 132, 104385.
- Liu, G.j., Xian, X.f., Zhou, J.p., Zhang, L., Liu, Q.l., Zhao, Y., Zhang, S.w., 2017. Experimental study on the supercritical co2 fracturing of shale. Journal of China Coal Society.

- Liu, Y., Yoshioka, K., You, T., Li, H., Zhang, F., 2024a. A phase-field fracture model in thermoporo-elastic media with micromechanical strain energy degradation. Computer Methods in Applied Mechanics and Engineering 429, 117165.
- Liu, Y., Yoshioka, K., You, T., Li, H., Zhang, F., 2024b. A phase-field fracture model in thermoporo-elastic media with micromechanical strain energy degradation. Computer Methods in Applied Mechanics and Engineering 429, 117165.
- Lu, M., Connell, L.D., 2014. The transient behaviour of co2 flow with phase transition in injection wells during geological storage—application to a case study. Journal of Petroleum Science and Engineering 124, 7–18.
- Luo, Z., Cheng, L., Zhao, L., Xie, Y., 2022. Numerical simulation and analysis of thermo-hydro mechanical behaviors of hydraulic fracturing in naturally fractured formation using a thm-xfem
   coupling model. Journal of Natural Gas Science and Engineering 103, 104657.
- Matter, J.M., Kelemen, P.B., 2009. Permanent storage of carbon dioxide in geological reservoirs by mineral carbonation. Nature geoscience 2, 837–841.
- 600 Maxwell, J.C., 1876. Capillary action. Encyclopaedia Britannica 5, 256–275.
- McWhorter, D.B., Sunada, D.K., 1990. Exact integral solutions for two-phase flow. Water Resources Research 26, 399–413.
- Middleton, R.S., Carey, J.W., Currier, R.P., Hyman, J.D., Kang, Q., Karra, S., Jiménez-Martínez,
   J., Porter, M.L., Viswanathan, H.S., 2015. Shale gas and non-aqueous fracturing fluids: Opportunities and challenges for supercritical co2. Applied Energy 147, 500–509.
- Miehe, C., Mauthe, S., 2016. Phase field modeling of fracture in multi-physics problems. part iii.
  crack driving forces in hydro-poro-elasticity and hydraulic fracturing of fluid-saturated porous
  media. Computer Methods in Applied Mechanics and Engineering 304, 619–655.
- Miehe, C., Mauthe, S., Teichtmeister, S., 2015. Minimization principles for the coupled problem of darcy-biot-type fluid transport in porous media linked to phase field modeling of fracture.

  Journal of the Mechanics and Physics of Solids 82, 186–217.
- Mikelić, A., Wheeler, M.F., Wick, T., 2015. A quasi-static phase-field approach to pressurized fractures. Nonlinearity 28, 1371.
- Mojid, M.R., Negash, B.M., Abdulelah, H., Jufar, S.R., Adewumi, B.K., 2021. A state-of-art review
   on waterless gas shale fracturing technologies. Journal of Petroleum Science and Engineering 196,
   108048.
- $_{617}$  Moridis, G., 2017. Literature review and analysis of waterless fracturing methods .
- Nianyin, L., Chao, W., Suiwang, Z., Jiajie, Y., Yinhong, D., et al., 2021. Recent advances in waterless fracturing technology for the petroleum industry: An overview. Journal of Natural Gas Science and Engineering 92, 103999.
- Noii, N., Wick, T., 2019. A phase-field description for pressurized and non-isothermal propagating fractures. Computer Methods in Applied Mechanics and Engineering 351, 860–890.

- Osiptsov, A.A., 2017. Fluid mechanics of hydraulic fracturing: a review. Journal of petroleum science and engineering 156, 513–535.
- Peng, D.Y., Robinson, D.B., 1976. A new two-constant equation of state. Industrial & Engineering
  Chemistry Fundamentals 15, 59–64.
- Qun, L., Dingwei, W., Jianhui, L., Yiliang, L., Xin, W., Baoshan, G., et al., 2019. Achievements and future work of oil and gas production engineering of cnpc. Petroleum Exploration and Development 46, 145–152.
- Schultz, R., Skoumal, R.J., Brudzinski, M.R., Eaton, D., Baptie, B., Ellsworth, W., 2020. Hydraulic
   fracturing-induced seismicity. Reviews of Geophysics 58, e2019RG000695.
- Song, X., Guo, Y., Zhang, J., Sun, N., Shen, G., Chang, X., Yu, W., Tang, Z., Chen, W., Wei, W.,
   et al., 2019. Fracturing with carbon dioxide: from microscopic mechanism to reservoir application.
   Joule 3, 1913–1926.
- Span, R., Wagner, W., 1996. A new equation of state for carbon dioxide covering the fluid region from the triple-point temperature to 1100 k at pressures up to 800 mpa. Journal of physical and chemical reference data 25, 1509–1596.
- Suh, H.S., Sun, W., 2021. Asynchronous phase field fracture model for porous media with thermally
   non-equilibrated constituents. Computer Methods in Applied Mechanics and Engineering 387,
   114182.
- Tanné, E., Li, T., Bourdin, B., Marigo, J.J., Maurini, C., 2018. Crack nucleation in variational phase-field models of brittle fracture. Journal of the Mechanics and Physics of Solids 110, 80–99.
- Vengosh, A., Jackson, R.B., Warner, N., Darrah, T.H., Kondash, A., 2014. A critical review of the
   risks to water resources from unconventional shale gas development and hydraulic fracturing in
   the united states. Environmental science & technology 48, 8334–8348.
- Wang, X., Li, P., Qi, T., Li, L., Li, T., Jin, J., Lu, D., 2023. A framework to model the hydraulic
   fracturing with thermo-hydro-mechanical coupling based on the variational phase-field approach.
   Computer Methods in Applied Mechanics and Engineering 417, 116406.
- Wheeler, M.F., Wick, T., Wollner, W., 2014. An augmented-lagrangian method for the phase-field
   approach for pressurized fractures. Computer Methods in Applied Mechanics and Engineering
   271, 69–85.
- Wu, L., Hou, Z., Luo, Z., Xiong, Y., Zhang, N., Luo, J., Fang, Y., Chen, Q., Wu, X., 2023.
   Numerical simulations of supercritical carbon dioxide fracturing: A review. Journal of Rock
   Mechanics and Geotechnical Engineering 15, 1895–1910.
- Xiao, F., Salimzadeh, S., Zhang, Q.B., 2024. A 3d coupled numerical simulation of energised
   fracturing with co2: Impact of co2 phase on fracturing process. International Journal of Rock
   Mechanics and Mining Sciences 182, 105863.
- Xie, W., Chen, S., Wang, M., Yu, Z., Wang, H., 2021. Progress and prospects of supercritical co2 application in the exploitation of shale gas reservoirs. Energy & Fuels 35, 18370–18384.

- Xu, W., Yu, H., Zhang, J., Lyu, C., Wang, Q., Micheal, M., Wu, H., 2022. Phase-field method
   of crack branching during sc-co2 fracturing: A new energy release rate criterion coupling pore
   pressure gradient. Computer Methods in Applied Mechanics and Engineering 399, 115366.
- Yan, H., Zhang, J., Zhou, N., Li, M., 2019. Staged numerical simulations of supercritical co2 fracturing of coal seams based on the extended finite element method. Journal of Natural Gas Science and Engineering 65, 275–283.
- Yan, H., Zhang, J., Zhou, N., Li, M., Suo, Y., 2020. Numerical simulation of dynamic interactions between two cracks originating from adjacent boreholes in the opposite directions during supercritical co2 fracturing coal mass. Engineering Fracture Mechanics 223, 106745.
- Yang, B., Wang, H.Z., Li, G.S., Wang, B., Chang, L., Tian, G.H., Zhao, C.M., Zheng, Y., 2022.
   Fundamental study and utilization on supercritical co2 fracturing developing unconventional
   resources: Current status, challenge and future perspectives. Petroleum Science 19, 2757–2780.
- Yang, R., Hong, C., Gong, Y., Huang, Z., Valizadeh, N., Zhou, S., Li, G., Zhuang, X., 2024. Phase field cohesive zone modeling of hydro-thermally induced fracture in hot dry rock during liquid
   nitrogen fracturing. Renewable Energy 223, 120070.
- Yang, W., Zhou, C., Qin, F., Li, D., 1992. High-energy gas fracturing (hegf) technology: research and application, in: SPE Europec featured at EAGE Conference and Exhibition?, SPE. pp. SPE-24990.
- Yew, C.H., Weng, X., 2014. Mechanics of hydraulic fracturing. Gulf Professional Publishing.
- Yi, D., Yi, L., Yang, Z., Meng, Z., Li, X., Yang, C., Zhang, D., 2024a. Coupled thermo-hydro mechanical-phase field modelling for hydraulic fracturing in thermo-poroelastic media. Computers
   and Geotechnics 166, 105949.
- Yi, L., Zhang, D., Yang, Z., Li, X., Liao, Z., Chen, J., 2024b. An improved phase-field model for oil—
   water two-phase flow and mixed-mode fracture propagation in hydraulic fracturing. Theoretical
   and Applied Fracture Mechanics 134, 104677.
- Yoshioka, K., Naumov, D., Kolditz, O., 2020. On crack opening computation in variational phasefield models for fracture. Computer Methods in Applied Mechanics and Engineering 369, 113210.
- You, T., Yoshioka, K., 2023. On poroelastic strain energy degradation in the variational phasefield models for hydraulic fracture. Computer Methods in Applied Mechanics and Engineering 416, 116305. URL: https://www.sciencedirect.com/science/article/pii/S0045782523004292, doi:https://doi.org/10.1016/j.cma.2023.116305.
- You, T., Yoshioka, K., 2025. Remote hydraulic fracturing at weak interfaces. Computers and
   Geotechnics 177, 106830.
- Zhang, C., Liu, S., Ma, Z., Ranjith, P., 2021. Combined micro-proppant and supercritical carbon
   dioxide (sc-co2) fracturing in shale gas reservoirs: A review. Fuel 305, 121431.
- Zhang, F., Damjanac, B., Maxwell, S., 2019a. Investigating hydraulic fracturing complexity in naturally fractured rock masses using fully coupled multiscale numerical modeling. Rock Mechanics and Rock Engineering 52, 5137–5160.

- Zhang, X., Lu, Y., Tang, J., Zhou, Z., Liao, Y., 2017. Experimental study on fracture initiation and propagation in shale using supercritical carbon dioxide fracturing. Fuel 190, 370–378.
- Zhang, X., Zhu, W., Xu, Z., Liu, S., Wei, C., 2022. A review of experimental apparatus for
   supercritical co2 fracturing of shale. Journal of Petroleum Science and Engineering 208, 109515.
- Zhang, Y., He, J., Li, X., Lin, C., 2019b. Experimental study on the supercritical co2 fracturing of
   shale considering anisotropic effects. Journal of Petroleum Science and Engineering 173, 932–940.
- Zhou, D., Zhang, G., Prasad, M., Wang, P., 2019. The effects of temperature on supercritical co2
   induced fracture: An experimental study. Fuel 247, 126–134.
- Zhou, D., Zhang, G., Wang, Y., Xing, Y., 2018. Experimental investigation on fracture propagation
   modes in supercritical carbon dioxide fracturing using acoustic emission monitoring. International
   Journal of Rock Mechanics and Mining Sciences 110, 111–119.
- Zhou, D.w., Zhang, G.q., 2020. A review of mechanisms of induced fractures in sc-co2 fracturing.
   Petroleum Science Bulletin 5, 239–253.
- Zhou, Q., Zhu, Z., Zhang, R., Fan, Z., Nie, X., Gao, W., Li, C., Wang, J., Ren, L., 2024. Rock
   fracture initiation under deep extreme in situ conditions: A review. Journal of Rock Mechanics
   and Geotechnical Engineering .
- Zhu, R., Tian, G., Qu, F., Li, N., Li, G., Long, C., Fan, X., 2024. Study on fracture propagation
   of hydraulic and supercritical co2 fracturing in different rock. Thermal Science, 32–32.
- Zou, Y., Li, N., Ma, X., Zhang, S., Li, S., 2018. Experimental study on the growth behavior of supercritical co2-induced fractures in a layered tight sandstone formation. Journal of Natural Gas Science and Engineering 49, 145–156.